Journal of Geochemical Exploration 198 (2019) 41–53

Contents lists available at ScienceDirect

Journal of Geochemical Exploration

journal homepage: www.elsevier.com/locate/gexplo

The Cu-Ni mineralization potential of the Kaimuqi mafic-ultramafic complex and the indicators for the magmatic Cu-Ni sulfide deposit exploration in the East Kunlun Orogenic Belt, Northern Qinghai-Tibet Plateau, China

YueGao Liu[a,*], ZhengGuo Chen[b], WenYuan Li[a,*], XunHui Xu[b], Xin Kou[b], QunZi Jia[a], ZhaoWei Zhang[a], Fang Liu[c], YaLei Wang[a], MinXin You[a]

[a] Key Laboratory for the Study of Focused Magmatism and Giant Ore Deposits, Ministry of Natural Resources, Xi'an Center of Geological Survey, China Geological Survey, Xi'an 710054, PR China
[b] Sino Shaanxi Nuclear Industry Group Geological Survey Co, Ltd, Xi'an 710100, PR China
[c] TBEA Co., Ltd., ChangJi 831100, PR China

ARTICLE INFO

Keywords:
East Kunlun Orogenic Belt
Kaimuqi mafic-ultramafic complex
Cu-Ni ore deposit
Late Triassic
Sulfide saturation
Exploration indicators

ABSTRACT

The East Kunlun Orogenic Belt experienced two periods of mantle-derived magmatic activity during its post-collisional stages. One occurred during the Late Silurian-Early Devonian, and the other occurred during the Middle-Late Triassic. The Late Silurian-Early Devonian Xiarihamu mafic-ultramafic intrusions were found to be associated with a giant magmatic sulfide Ni-Co deposit discovered in 2012. The U-Pb age of websterite in the Kaimuqi mafic-ultramafic intrusion is 221.1 ± 2.3 Ma. None of the Middle-Late Triassic mafic-ultramafic intrusions in the East Kunlun Orogenic Belt contain Cu-Ni mineralization. Based on simulations by the software MELTS, we found that the crystallization process leads to a drop in the sulfur content at sulfide saturation. The mineralized Late Silurian-Early Devonian mafic-ultramafic intrusions exhibit both a broader range of m/f values and higher m/f values than the non-mineralized intrusions in the East Kunlun Orogenic Belt, which means that the mineralized intrusions experienced a long process of crystallization differentiation. This process is probably responsible for Cu-Ni mineralization in the Early Devonian Xiarihamu mafic-ultramafic intrusion. Compared to the olivine and clinopyroxene in the Xiarihamu giant Cu-Ni deposit, the Late Triassic Kaimuqi olivine contains significantly lower MgO, Fo and SiO_2 contents and higher CaO and FeO contents, and the Kaimuqi clinopyroxene contains higher FeO and CaO contents. Therefore, we infer that the Kaimuqi intrusion formed from a melt with higher FeO and CaO contents and a lower SiO_2 content. This melt required more sulfur to achieve sulfide saturation. This characteristic most likely hindered mineralization in the Kaimuqi mafic-ultramafic intrusion. All of the mafic-ultramafic intrusions that host Cu-Ni deposits in the East Kunlun Orogenic Belt contain lherzolite, harzburgite, and orthopyroxenite, indicating that the pyroxene in these intrusions is mainly the orthopyroxene. If an intrusion contains more clinopyroxene, it indicates that its magma contains more calcium. The magma with higher calcium content will need a higher sulfur content to achieve sulfide saturation. Although websterite occurred in the Kaimuqi intrusion, the clinopyroxene and orthopyroxene content in the websterite is 75% and 20%, respectively, and the peridotite lithofacies is wehrlite. Therefore, orthopyroxene is rare in the Kaimuqi mafic-ultramafic intrusions. Thus, the Kaimuqi mafic-ultramafic intrusion may not have had the potential to form Cu-Ni ore deposits. Finally, this paper summarizes some geological and geochemical indicators for Cu-Ni mineralization in the mafic-ultramafic intrusions in the East Kunlun Orogenic Belt. These indicators provide some enlightenment to the exploration of Cu-Ni deposits in mafic-ultramafic intrusions, especially for the geological exploration bureaus or companies, which do not have the budget for large numbers of geological dating, isotopes, major elements, and platinum group elements during the exploration evaluation process in the current global mining recession situation.

* Corresponding authors.
E-mail addresses: ltdzgj_2006@126.com (Y. Liu), xalwenyuan@126.com (W. Li).

https://doi.org/10.1016/j.gexplo.2018.12.002
Received 6 March 2018; Received in revised form 9 November 2018; Accepted 9 December 2018
Available online 17 December 2018

1. Introduction

Many well-known magmatic Cu-Ni-PGE sulfide deposits in the world are found in mafic-ultramafic intrusions, such as the Jinchuan Cu-Ni-PGE deposit (Tang et al., 2005, 2007; Lehmann et al., 2007; Song et al., 2009; Zhang et al., 2010; Li and Ripley, 2011; Duan et al., 2016; Yang et al., 2018) and the Xiarihamu Cu-Ni in China (Jiang et al., 2015; Li et al., 2015; Song et al., 2016; Zhang et al., 2017; Liu et al., 2018), the J-M PGE reef in Stillwater complex in USA (Page, 1971; Barnes and Naldrett, 1985; Wall and Scoates, 2016), the Voisey's Bay Ni-Cu-Co deposit (Lightfoot and Naldrett, 1999; Naldrett et al., 2000; Ripley et al., 2000; Lightfoot et al., 2012; Hiebert et al., 2013) and the Mascot Ni-Cu-PGE deposit in Canada (Nixon, 2002; Manor et al., 2014; Manor et al., 2016), and so on. However, most of the world's mafic-ultramafic intrusions are not mineralized. Two common features of some mafic-ultramafic intrusions hosting Cu-Ni-PGE ore deposits are: (1) the obvious differentiation from ultramafic rocks to mafic rocks, even to intermediate rocks; (2) a large amount of orthopyroxene existed, and the content of orthopyroxene is obviously larger than that of clinopyroxene. For example, the lithofacies in the Stillwater complex include dunite, bronzitites, norite, gabbronorite, troctolite, and anorthosite, and the sulfides are hosted in norite and cumulate bronzitites (Barnes and Naldrett, 1985). The orthorhombic crystallization promotes the formation of the J-M PGE reef in the Stillwater complex (Raedeke and Vian, 1986; Zientek et al., 2002). The Cu-Ni deposits in the East Kunlun Orogenic Belt (EKOB) in this study also have these two characteristics. The EKOB experienced two periods of mantle-derived magmatic activity occurred in the post-collisional geological setting: one occurred during the Late Silurian-Early Devonian (Zhu et al., 2006; B. Liu et al., 2012, 2013a), and the other occurred during the Middle-Late Triassic (Luo et al., 2002; Feng et al., 2012; Chen et al., 2013; Li et al., 2014; B. Liu et al., 2014; Luo et al., 2014; Wang et al., 2014; Xiong et al., 2014a). During these periods of mantle-derived magmatic activity, many mafic-ultramafic intrusions formed. The mafic-ultramafic intrusions produced during the Late Silurian to the Early Devonian include the Xiarihamu and Binggounan intrusions (Wang, 2014; Li et al., 2015; Song et al., 2016; Liu et al., 2018); the representative mafic-ultramafic intrusions produced during the Middle-Late Triassic are the Xiaojianshan and Lalingaoli intrusions (Ao et al., 2015). Some of the Late Silurian-Early Devonian mafic-ultramafic intrusions contains significant Cu-Ni sulfides, such as the Xiarihamu giant Cu-Ni deposit. The Xiarihamu Cu-Ni sulfide deposit contains ~157 million metric tons (Mt) of sulfide ores with average metal grades of 0.65 wt% Ni, 0.14 wt% Cu, and 0.013 wt% Co (No. 5 GMSQH, 2014). This makes the Xiarihamu deposit not only the second-largest Ni deposit in China (after Jinchuan) but also one of the largest Ni deposits in an orogenic setting in the world (Li et al., 2012; Song et al., 2016; Liu et al., 2018). The discovery of the Xiarihamu giant Cu-Ni deposit in 2012 has led to an increase in the number of studies on the mafic-ultramafic intrusions in the EKOB. However, only some of the Late Silurian-Early Devonian mafic-ultramafic intrusions and none of the Middle-Late Triassic mafic-ultramafic intrusions contain Cu-Ni mineralization. No systematic studies or mineralization potential evaluations have been conducted on the Kaimuqi mafic-ultramafic complex by any research team. Therefore, in this paper, we used petrographic, geochronologic, Sr-Nd-Hf isotopic and mineralogical methods to gain a better understanding of the Kaimuqi mafic-ultramafic intrusion. By comparing all of the geological and geochemical features described above with those of the Xiarihamu Cu-Ni deposit, we evaluated the metallogenic potential of the Kaimuqi intrusion and summarized the geological and geochemical indicators for Cu-Ni mineralization in the mafic-ultramafic intrusions in the EKOB.

Although magmatic origin, whether sulfide liquid settled out of magma prior to emplacement or not, and crustal sulfur contamination are important for the Cu-Ni deposits formation in the mafic-ultramafic intrusions (Barnes et al., 1993; Barnes and Lightfoot, 2005; Lightfoot and Milkereit, 2007; Mao et al., 2008; Naldrett, 2011; Wei et al., 2013; Liu et al., 2016, 2017; Lacono-Marziano et al., 2017), this paper attempts to analyze the metallogenic potential of mafic-ultramafic intrusions the EKOB from the perspective of lithofacies differentiation and mineralogy. In the current global mining recession situation, geological exploration bureaus or companies in China do not have the budget for the test of a large number of geological dating, isotopes, major elements, and platinum group elements during the exploration evaluation. Therefore, it is necessary to summarize some indicators from basic lithofacies and mineralogy.

2. Geologic background

The Kaimuqi mafic-ultramafic complex is located in the EKOB, which is located in the northern region of the Qinghai-Tibet Plateau (Fig. 1a). The EKOB is located in the western region of the central orogenic belt in mainland China (Fig. 1a). This belt is bordered by the Qaidam Block to the north and the Bayan Har-Sonpanganzi Terrane to the south (Fig. 1). The EKOB trends E-W and is approximately 1500 km long and 50–200 km wide. The belt is cut by three closely related, deep, E-W-trending regional faults: from north to south, the Northern Kunlun

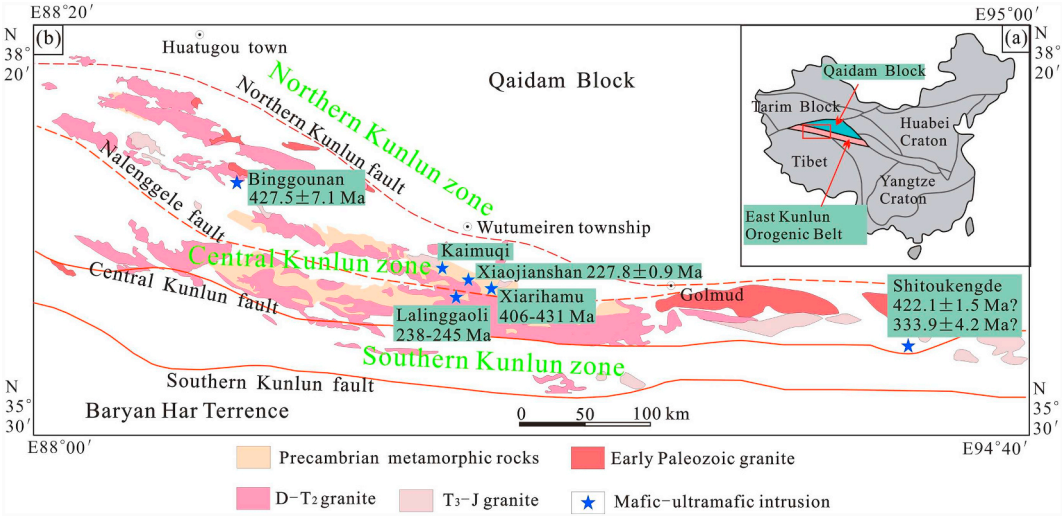

Fig. 1. (a). Tectonic sketch map of China. (b). Simplified tectonic units of the East Kunlun Orogenic Belt (modified after Xiao et al. (2014)). Binggounan age (Wang, 2014); Xiaojianshan age (Ao et al., 2015); Xiarihamu age (Li et al., 2015; Song et al., 2016); Shitoukengde age: 333.9 ± 4.2 Ma (Zhang et al., 2018), 422.1 ± 1.5 Ma (Li et al., 2018); Lalinggaoli age (Wang et al., 2017).

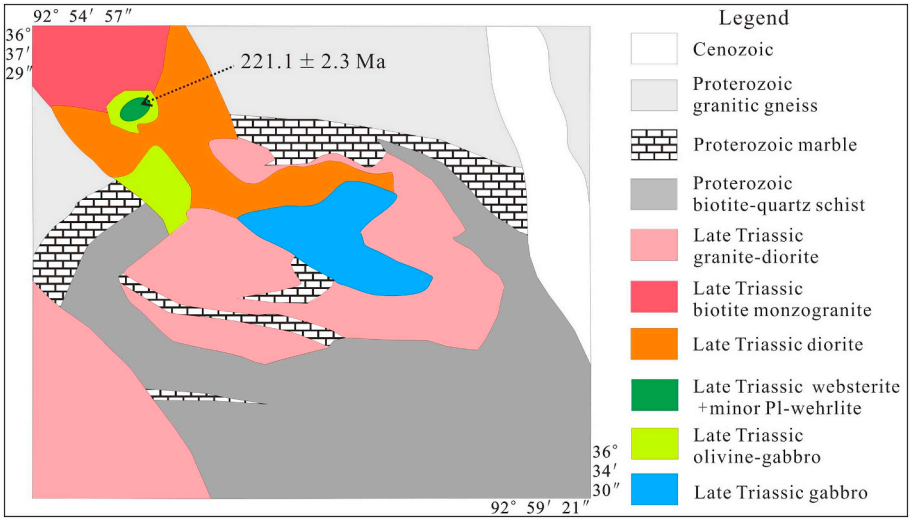

Fig. 2. Geologic map of the Kaimuqi mafic-ultramafic complex.
(Modified from Sino Shaanxi Nuclear Industry Group Geological Survey Co, Ltd, 2014). Age data are from this paper.

fault, the Central Kunlun fault, and the Southern Kunlun fault (Fig. 1b) (Huang et al., 1984; Jiang et al., 1992). The EKOB can be further divided into the Southern, Central, and Northern Kunlun zones by the Central Kunlun fault and the Northern Kunlun fault (Fig. 1b).

The exposed rocks in the Central Kunlun zone include the Proterozoic Baishahe Formation, Neoproterozoic granitic gneiss, the Upper Silurian to Lower Devonian Qimantage Group, the Upper Devonian Maoniushan Formation, the Lower Carboniferous Dagangou Formation, the Upper Triassic Elashan Formation and Cenozoic sediments (QGS, 2012; No. 5 GMSQH, 2014). In the Kaimuqi area, the Proterozoic Baishahe Formation is composed of granitic gneiss, biotite-quartz schist, and marble.

The Central Kunlun Fault represents the remains of a small Early Paleozoic oceanic basin; the youngest age from the Qingshuiquan ophiolite complexes in the Central Kunlun region is 508 Ma (Li et al., 2006). Furthermore, an arc-related granite in the East Kunlun region has been dated to 508 Ma (CUG, 2003). Therefore, the East Kunlun region entered an oceanic subduction stage after 508 Ma (Mo et al., 2007). The tectonic transition from oceanic subduction to continent-continent collision occurred at 438 Ma (B. Liu et al., 2013a). The eclogites in the Wenquan area of the Central Kunlun Fault, which have been dated to 428 Ma, are associated with this continent-continent collisional event (Meng et al., 2013).

In the EKOB, considerable mantle-related magmatic activity occurred after 428 Ma (Fig. 1b, c). The products of this activity include Middle-Upper Silurian (428–419 Ma) basalt (Zhu et al., 2006; QGS, 2012), Lower-Middle Devonian (411.5–382.8 Ma) mafic dykes (Sun et al., 2004; Xiong et al., 2014b; Yang et al., 2014), and Upper Silurian-Middle Devonian (419.0–391.1 Ma) A_2-type granite (Chen et al., 2013; B. Liu et al., 2013b; Wang et al., 2013; Gan, 2014; Yan et al., 2016). This mantle-related magmatic activity was produced in a post-collisional environment (B. Liu et al., 2012, 2013b; Gan, 2014; Peng et al., 2016; Song et al., 2016).

The formation of the early Carboniferous Buqingshan ophiolite in the Southern Kunlun Fault has been interpreted to mark the opening of the Late Paleozoic Kunlun ocean basin (Chen et al., 2003; Yang et al., 2004).

Subduction-associated magmatic rocks were mainly produced from the Middle-Late Permian to the Middle Triassic (227–260 Ma); these rocks are distributed mainly in the Central Kunlun zone and have a tendency to decrease in abundance from south to north (Mo et al., 2007; Wang et al., 2014). The Late Permian granite assemblage formed in a continental margin arc setting, probably due to the subduction of the Paleo-Tethys Ocean; in contrast, the widespread Middle Triassic granites formed during a subduction-collisional conversion stage due to the break-off of the subducting lithospheric slab (Wang et al., 2014). The East Kunlun region entered a post-collisional stage during the Late Triassic and formed a rock assemblage comprising A-type granites, mafic dykes and mafic-ultramafic intrusions produced by mantle-derived magmatic activity (Feng et al., 2012; B. Liu et al., 2014; Wang et al., 2014; Ao et al., 2015).

In summary, the EKOB experienced two periods of mantle-derived magmatic activity during its post-collisional stages; one occurred during the Late Silurian-Early Devonian, and the other occurred during the Middle-Late Triassic (Luo et al., 2002; Mo et al., 2007). The Xiarihamu giant Cu-Ni deposit (406–431 Ma) (Li et al., 2015; Song et al., 2016; Zhang et al., 2017; Liu et al., 2018), which were produced by Late Silurian-Early Devonian mantle-derived magmatic activity, are located in the Central Kunlun zone (Fig. 1b). These two periods of mantle-derived magmatic activity also produced some non-mineralized mafic-ultramafic intrusions, such as the Binggounan (427.5 Ma), Xiaojianshan (227.8 Ma) and Lalinggaoli (238–245 Ma) intrusions (Wang, 2014; Ao et al., 2015; Wang et al., 2017). The Kaimuqi mafic-ultramafic complex is also located in the Central Kunlun zone, 41 km to the northwest of the Xiarihamu giant Cu-Ni deposit.

3. Geology of the Kaimuqi intrusion

The strata in the study area are composed mainly of Proterozoic granitic gneiss, biotite-quartz schist and marble (Fig. 2). The Kaimuqi mafic-ultramafic complex consists mainly of three intrusions, which from the southeast to the northwest are composed of gabbro, olivine gabbro, and websterite (the websterite intrusion includes a very small amount of plagioclase wehrlite) (Fig. 2). The websterite is located within the olivine gabbro, and it covers an area of approximately 0.06 km^2. Late Triassic biotite monzogranite, granite diorite, and diorite are also exposed around the Kaimuqi mafic-ultramafic complex. The contact boundary between the olivine gabbro and websterite features a chilled border in the olivine gabbro (Fig. 3a), confirming that the olivine gabbro formed later than the websterite. The biotite monzogranite also has chilled border when it contacts with the olivine gabbro (Fig. 3b). Thus, the biotite monzogranite formed later than the olivine gabbro.

The plagioclase wehrlite contains approximately 40% olivine (Ol), 45% clinopyroxene (Cpx), 10% plagioclase (Pl), approximately 2–5% amphibole, and 0.5% chromite (Fig. 4a). No sulfides were found in the plagioclase wehrlite.

The clinopyroxene (Cpx) content in the websterite is 75% (Fig. 4b).

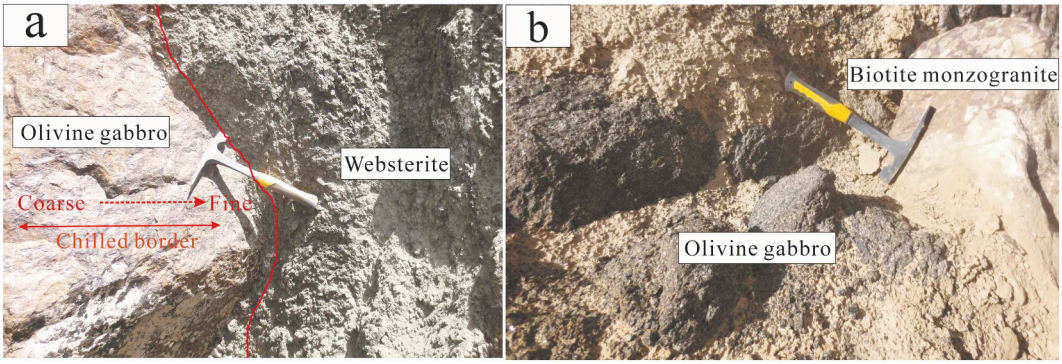

Fig. 3. Contact relationships between the major lithofacies (A: chilled border in the olivine gabbro; B: chilled border in the biotite monzogranite).

The clinopyroxene grains are platy and have dimensions of 0.5 × 1 mm, with some reaching sizes of up to 2–2.5 mm. The orthopyroxene (Opx) and plagioclase (Pl) contents in the websterite are 20% and 5%, respectively. The orthopyroxene and plagioclase grains are approximately 0.3 mm in diameter (Fig. 4b). Most of the websterite contains no sulfides, although a minor amount contains sparse disseminated sulfides (0.1–0.2%) located in the interstitial spaces between pyroxene grains. These sulfides mainly include pentlandite (Pn), pyrrhotite (Po), and chalcopyrite (Ccp) (Fig. 4c).

4. Analytical methodology

4.1. U-Pb dating

The U-Pb dating and trace element analyses of zircon collected from the websterite were conducted synchronously using laser ablation inductively coupled plasma mass spectrometry (LA-ICP-MS) at the Wuhan Sample Solution Analytical Technology Co., Ltd. The detailed operating conditions for the laser ablation system, the ICP-MS instrument and the data reduction process are described in Hu et al. (2008, 2012) and Liu et al. (2008, 2010). Time-dependent drifts of U-Th-Pb isotopic ratios were corrected using a linear interpolation (with time) for every five analyses (*i.e.* 91,500 + six zircon samples + 91,500) according to the variations of the 91,500 zircon standard and preferred U-Th-Pb isotopic ratios used for 91,500 are from (Wiedenbeck et al., 1995). Zircon standards GJ-1 (Jackson et al., 2004) and Plešovice (Sláma et al., 2008) were used as unknown samples to monitor the stability and accuracy of acquired U-Pb data. The uncertainty associated with the preferred values of the 91,500 external standard was propagated throughout the ultimate results. Concordia diagrams and weighted mean calculations were made using Isoplot/Ex_v.3 (Ludwig, 2003). The preferred elemental concentration values of the USGS reference glasses were taken from the GeoReM database (http://georem.mpch-mainz.gwdg.de/).

4.2. In situ Hf isotopic analyses

In situ zircon Hf isotopic analyses were performed using a Geolas Pro laser ablation system coupled to a Neptune multi-collector ICP-MS at the Key Laboratory for the Study of Focused Magmatism and Giant Ore Deposits, MLR, at the Xi'an Center of Geological Survey, China Geological Survey. The detailed instrumental conditions and data acquisition procedures are similar to those described by Hou et al. (2007) and Meng et al. (2014). A stationary laser ablation spot with a beam diameter of 30 μm was used for these analyses. The ablated aerosol was carried by helium and combined with argon in a mixing chamber before being introduced to the ICP-MS plasma. All of the Hf analyses were performed on the same spots that underwent U-Pb laser ablation analysis. The GJ-1 zircon standard was used as a reference standard; during this study, it yielded a weighted mean $^{176}Hf/^{177}Hf$ ratio of 0.282030 ± 40 (2SE).

4.3. Sr-Nd isotopes

High-precision Sr and Nd isotopic measurements were obtained at the Nanjing Focus MS Technology Co., Ltd. Geological rock powders were decomposed in high-pressure PTFE bombs. Sr and Nd were purified from the same digestion solution. An exchange column containing BioRad AG50W × 8 and Sr Spec resins were used to separate Sr, rare earth elements (REEs) and Pb from the sample matrix. Neodymium was separated from the other REEs in a second column using Ln Spec-coated Teflon powder. The Sr- and Nd-bearing elution was dried down and redissolved in 1.0 ml of 2 wt% HNO_3. Small aliquots of each sample were analyzed using an Agilent Technologies *7700*× quadrupole Multiple Collector Inductively Coupled Plasma mass spectrometry (MC-ICP-MS) (Hachioji, Tokyo, Japan) to determine the exact contents of Sr and Nd. Each diluted solution (containing 50 ppb Sr and 50 ppb Nd and doped with 10 ppb Tl) was introduced into a Nu Instruments *Nu Plasma II* multi-collector ICP-MS (Wrexham, Wales, UK) by a Teledyne Cetac

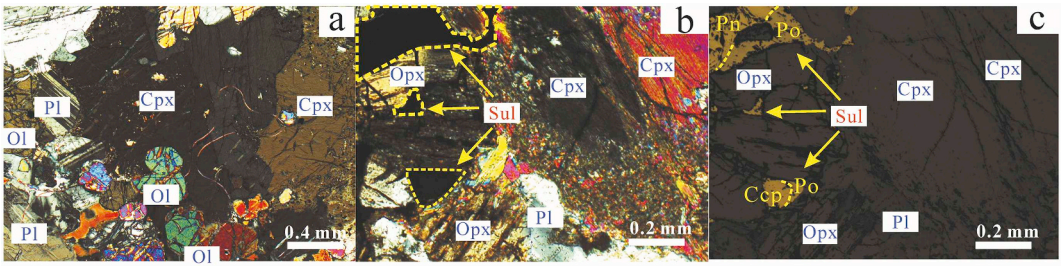

Fig. 4. Photomicrographs of the main rock types in the Kaimuqi mafic-ultramafic complex. Ol = olivine, Sul = sulfides, Opx = orthopyroxene, Cpx = clinopyroxene, Po = pyrrhotite, Pn = pentlandite, Ccp = chalcopyrite, and Pl = plagioclase.
a. Photomicrograph of plagioclase wehrlite; b. photomicrograph of websterite under transmitted light; c. photomicrograph of websterite under reflected light.

Technologies Aridus II desolvating nebulizer system (Omaha, Nebraska, USA). The raw isotopic ratios were corrected for mass fractionation by normalizing to values of $^{86}Sr/^{88}Sr = 0.1194$ for Sr and $^{146}Nd/^{144}Nd = 0.7219$ for Nd using an exponential law. International isotopic standards (NIST SRM 987 for Sr and JNdi-1 for Nd) were periodically analyzed to correct for instrumental drift. The USGS geochemical reference materials BCR-2, BHVO-2, AVG-2, and RGM-2 were analyzed for quality control. The Sr isotopic ratios obtained following the chemical pre-treatment and mass spectrometry procedures described above are consistent with the reported values within error (Weis et al., 2013).

4.4. Major element compositions of minerals

Mineral compositions were determined using a JXA-8100 electron microprobe at Chang'an University. The analytical conditions included an energy of 15 kV, a beam current of 20 nA, a beam diameter of 1–5 μm and a peak-counting time of 20 s. The standard materials used in the analysis were: albite, K-feldspar, hematite, forsterite, xenotime, pyrophanite, corundum, wollastonite, Cr-spinel, kynite, pyrophanite, metallic nickel, and metal zinc, respectively. All the materials are according to the National Standard of the People's Republic of China (1998). The standard title is the general specification of X-ray EDS Quantitative analysis for EPMA and SEM. The standard number is GB/T17359-1998. The lower limits of detection for all the elements under such conditions are 0.01%. The relative analytical error was ± 2%.

5. Results

5.1. Geochronology

The zircon grains from all samples are transparent, mostly subhedral, and 100–300 μm in length. The internal structures of the zircon crystals selected from the websterite were studied using cathodoluminescence images (Fig. 5). Some of the grains exhibit concentric zoning, for example, the points 4, 6, 7, 13, and 14 in Fig. 5, whereas some grains do not show clear concentric zoning, for example, the points 8 and 12 in Fig. 5. The width of the concentric zone in zircon are related to the temperature of the magma when zircon crystallizes: rapid diffusion of trace elements in high-temperature condition often forms a broader concentric zoning (such as zircon in mafic-ultramafic rocks); under low-temperature condition, the slow diffusion of trace elements generally forms a narrow magmatic annulus (such as zircon in type I and S granites) (Rubatto and Gebauer, 2000). The zircon concentric zone is very wide at high temperature, and the zircon cross-section exposed in points 8 and 12 in Fig. 5 perhaps is the plane which is parallel with a concentric zone. Therefore, these two grains do not show concentric zoning. All zircons yield nearly a same age. We believe that all the grains are magmatic zircons. The analytical results of the selected zircon crystals are listed in Table 1. The concordia plots produced from these analyses are shown in Fig. 6. These zircons have U, Th, and Pb concentrations of 716–2027 ppm, 636–3832 ppm and 99–357 ppm, respectively, and their Th/U ratios range from ~0.70–2.56. The Th/U ratio of magmatic zircon is generally greater than 0.4; whereas the Th/U of metamorphic zircon is less than 0.1 (Rubatto and Gebauer, 2000; Moller et al., 2003). This is consistent with our judgment that all the grains are magmatic zircons. All analyses yield concordant U-Pb ages, within analytical error; thus, the websterite yields a concordia age of 221.1 ± 2.3 Ma (MSWD = 0.2) (Fig. 6).

5.2. Lutetium-Hafnium (Lu-Hf) isotopes

The Lu-Hf isotopic compositions of the zircon crystals from the websterite in the Kaimuqi intrusion are listed in Table 2. The calculated εHf(t) values of these zircon crystals range from −0.74 to 3.51, with an average value of 1.09. Additionally, the εHf(t) values of the zircon crystals from the Xiarihamu websterite and plagioclase-bearing websterite range from 0.9 to 4.7, with an average value of 2.5 (Li et al., 2015). Thus, the εHf(t) values of the zircon crystals in the Kaimuqi websterite are similar to those in the Xiarihamu websterite and plagioclase-bearing websterite. The zircon single-stage Hf model ages (T(DM1)) and the two-stage Hf model ages (T(DM2)) from the Kaimuqi websterite are 731–896 Ma and 1033–1316 Ma, respectively (Table 2).

5.3. Strontium-Neodymium (Sr-Nd) isotopes

The Rb-Sr and Sm-Nd isotopic data are listed in Table 3. The initial isotopic ratios of the Kaimuqi websterite were calculated using a zircon U-Pb age of 221.1 Ma. The $(^{87}Sr/^{86}Sr)_i$ ratios of the Kaimuqi websterite range from 0.709047 to 0.709818, with an average value of 0.709433 (Fig. 7), and the $(^{87}Sr/^{86}Sr)_i$ values of the Xiarihamu orthopyroxenite range from 0.706426 to 0.708995, with an average value of 0.708132. The εNd(t) values of the Kaimuqi websterite range from −4.1 to −5.1, with an average value of −4.6, and the εNd(t) values of the Xiarihamu orthopyroxenite range from −3.2 to −4.0, with an average value of −3.6 (Fig. 7).

5.4. Major element compositions of minerals

All of the major element compositions of olivine and clinopyroxene are listed in Supplementaries 1 and 2, respectively.

The MgO, Fo, NiO, SiO_2, CaO, and FeO contents of the Kaimuqi olivine are 37.948–44.583%, 74.86–84.77, 0.06–0.102%, 37.759–39.738%, 0.022–0.133%, and 13.777–22.888%, respectively, whereas those of the Xiarihamu olivine are 43.4–49.03%, 81.95–89.90, 0.07–0.61%, 38.41–41.02%, 0–0.09%, and 10.49–16.86%, respectively. Compared with the Xiarihamu olivine, the Kaimuqi olivine contains significantly lower contents of MgO, NiO, Fo, and SiO_2 but higher contents of CaO and FeO (Fig. 8). We also find the olivine composition difference between the contemporary no mineralized Binggounan mafic-ultramafic intrusions and the Giant Xiarihamu Cu-Ni deposit. The MgO, Fo, SiO_2, CaO, and FeO contents of the Binggounan olivine are 41.12–44.69%, 79.14–83.59, 38.03–40.07%, 0.08–0.25%, and 15.35–19.03%, respectively. Thus, the Binggounan olivine also contains lower contents of MgO, Fo, and SiO_2 but higher contents of CaO and FeO than the Xiarihamu olivine (Fig. 8).

The MgO, FeO, CaO, and SiO_2 contents of the Kaimuqi clinopyroxene range from 14.654–15.978%, 3.202–6.356%, 21.261–23.968%, and 49.731–53.086%, respectively, whereas those of the Xiarihamu clinopyroxene range from 14.79–17.60%, 3.69–5.93%, 12.306–23.820% and 48.78–52.32%, respectively. The average MgO, FeO, CaO, and SiO_2 contents of the Kaimuqi clinopyroxene are 15.427%, 5.205%, 22.392%, and 51.723%, respectively, whereas these of the Xiarihamu clinopyroxene are 16.34%, 4.08%, 19.54%, and 51.31%, respectively. Therefore, the Kaimuqi clinopyroxene contains similar contents of MgO and SiO_2 as the Xiarihamu clinopyroxene, but it contains higher FeO and CaO contents than the Xiarihamu clinopyroxene (Fig. 8).

6. Discussion

All of the mineralized mafic-ultramafic intrusions in the EKOB are Late Silurian-Early Devonian in age (Table 4). None of the Middle-Late Triassic and only some of the Late Silurian-Early Devonian mafic-ultramafic intrusions have been mineralized. The U-Pb age of the Kaimuqi websterite is 221.1 ± 2.3 Ma (n = 14, MSWD = 0.2; Fig. 6). Thus, the Kaimuqi mafic-ultramafic intrusion may not have had the potential to form a Cu-Ni ore deposit.

The two periods mantle-derived magmatic activity occurred in the post-collisional geological setting in the EKOB was probably related to the upwelling of the asthenosphere caused by the slab break-off (Luo et al., 2002; Mo et al., 2007; Chen et al., 2013; Zhang et al., 2014; Liu et al., 2018). The εHf(t) values of the gabbro from the Xiarihamu II intrusion range from 6.0–12.9, with an average value of 10.9 (Peng

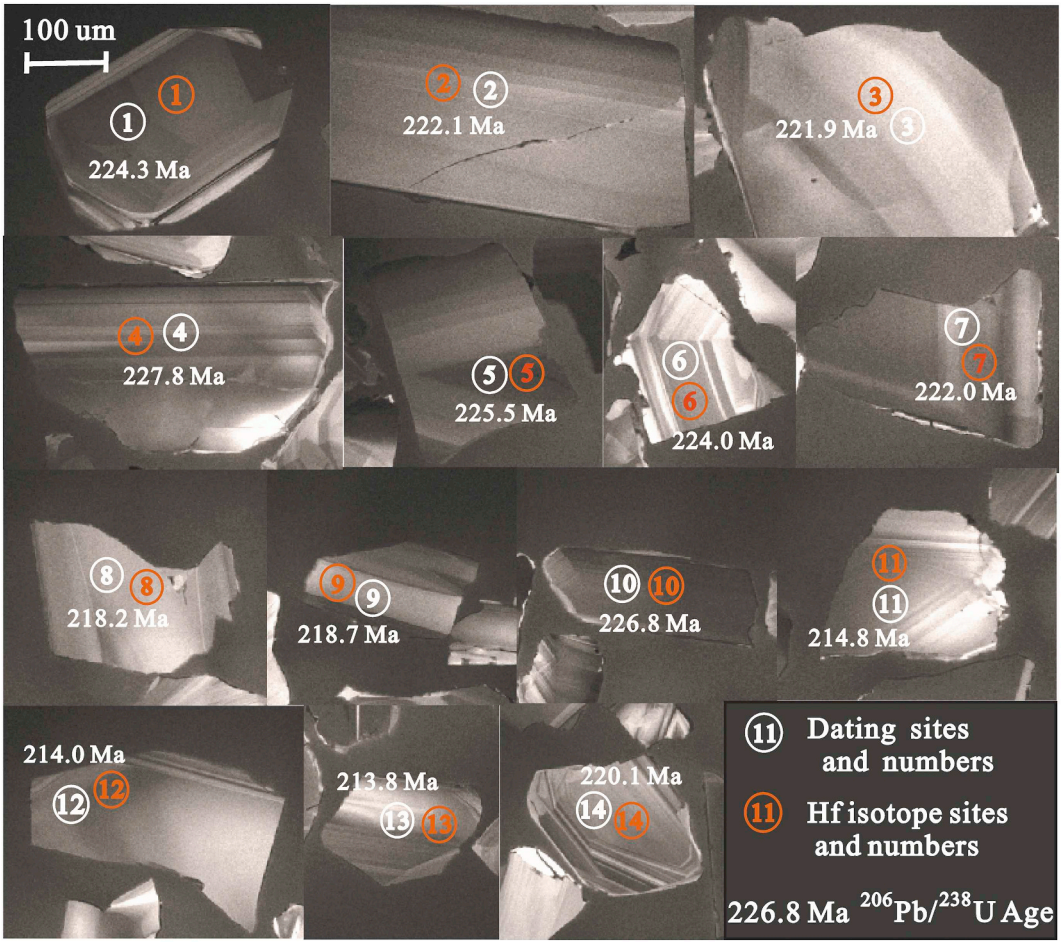

Fig. 5. Cathodoluminescence images of selected zircons from the Kaimuqi websterite.

et al., 2016). These high εHf(t) values and all of the Sr-Nd isotopic values of the orthopyroxenite plot near the EM-2 field (Fig. 7), which indicates that the Xiarihamu intrusion is unlikely to have been derived from the continental lithospheric mantle, which is characterized by εHf (t) values of less than 0 (Griffin et al., 2000) and plots near the EM-1 field on the ($^{87}Sr/^{86}Sr)_i$ - εNd(t) diagram (Basu et al., 1991; Jiang et al., 2005; Ye et al., 2013). Consequently, most of the researchers including the experts who discovered the Xiarihamu Ni deposit conclude that the Xiarihamu mafic-ultramafic intrusions were derived from the asthenospheric mantle (Li et al., 2012; Ao, 2014; Wang, 2014; Peng et al., 2016). The 213 Ma high Nb-Ta rhyolite (Ding et al., 2011), the 215 Ma adakite-like high-Mg diorite dike (Ding et al., 2014), and the 218 Ma late Triassic mafic dikes in the EKOB (Hu et al., 2016), was produced by the asthenospheric upwelling. Therefore, the Kaimuqi 221 Ma websterite with higher Mg content than the above rocks perhaps also derived from the asthenospheric mantle. The εHf(t) values of the websterite from the Xiarihamu and Kaimuqi are much lower than that of the typical gabbro derived from the asthenospheric mantle and the εNd(t) values are lower than the MORB in the EKOB (Fig. 7), are probably due to crustal contamination.

Table 1
LA-ICP-MS U-Pb age data of zircons from websterite.

No.	Pb(total)	Th	U	Th/U	Pb (common)	$^{207}Pb/^{235}U$		$^{208}Pb/^{232}Th$		$^{206}Pb/^{238}U$		$^{207}Pb/^{235}U$		$^{208}Pb/^{232}Th$		$^{206}Pb/^{238}U$	
	ppm	ppm	ppm		ppm	Ratio	1σ	Ratio	1σ	Ratio	1σ	Age (Ma)	1σ	Age (Ma)	1σ	Age (Ma)	1σ
1	357.15	2478.53	1095.56	2.26	4.09	0.2550	0.0128	0.0177	0.0008	0.0354	0.0005	230.62	10.38	354.21	16.62	224.32	3.25
2	150.24	888.19	1260.18	0.70	9.21	0.2983	0.0140	0.0188	0.0010	0.0350	0.0005	265.04	10.93	377.24	20.14	222.07	3.16
3	106.15	727.21	715.58	1.02	0.00	0.2690	0.0167	0.0191	0.0011	0.0350	0.0006	241.89	13.40	381.90	21.84	221.88	3.58
4	177.12	1271.20	924.09	1.38	11.25	0.2956	0.0180	0.0197	0.0012	0.0360	0.0006	262.97	14.09	393.91	23.04	227.80	3.44
5	173.58	1111.42	1451.52	0.77	0.00	0.2627	0.0134	0.0178	0.0010	0.0356	0.0004	236.88	10.76	357.24	19.45	225.45	2.79
6	201.41	1412.66	1307.77	1.08	14.18	0.2595	0.0134	0.0149	0.0007	0.0354	0.0005	234.27	10.83	299.32	14.61	223.96	2.81
7	515.25	3831.70	2026.86	1.89	1.83	0.2403	0.0128	0.0132	0.0006	0.0350	0.0005	218.69	10.44	265.73	11.40	222.04	2.88
8	168.36	1285.87	722.95	1.78	0.00	0.2160	0.0166	0.0103	0.0004	0.0344	0.0006	198.56	13.88	207.32	8.48	218.16	3.53
9	99.20	636.45	775.85	0.82	0.00	0.2173	0.0215	0.0097	0.0007	0.0345	0.0007	199.63	17.95	194.52	14.26	218.68	4.42
10	133.00	916.11	915.98	1.00	26.89	0.2252	0.0142	0.0084	0.0003	0.0358	0.0006	206.26	11.80	169.20	6.94	226.79	3.45
11	219.46	1560.63	1374.17	1.14	63.57	0.2120	0.0126	0.0086	0.0003	0.0339	0.0005	195.23	10.53	174.00	6.57	214.67	2.86
12	418.76	3332.70	1303.16	2.56	0.54	0.2107	0.0108	0.0086	0.0003	0.0337	0.0005	194.10	9.06	172.39	6.49	213.94	3.08
13	297.41	2261.37	1501.42	1.51	25.14	0.2157	0.0103	0.0088	0.0004	0.0337	0.0005	198.34	8.59	176.84	7.47	213.78	3.42
14	243.20	1797.07	1392.56	1.29	14.13	0.2183	0.0106	0.0088	0.0004	0.0348	0.0005	200.52	8.84	176.55	8.22	220.59	2.94

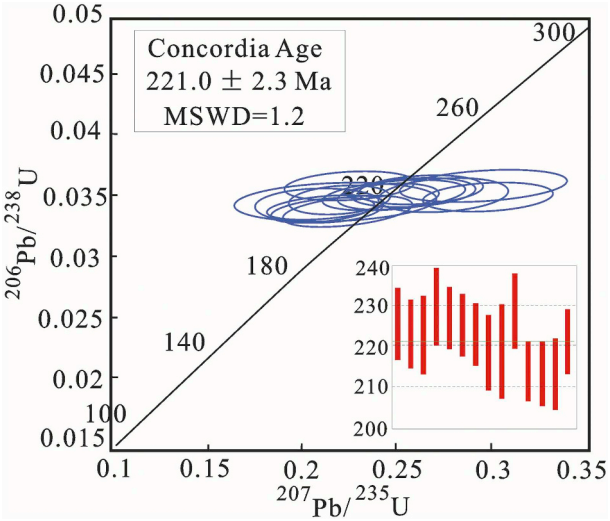

Fig. 6. Zircon U-Pb isotope concordia plot for websterite in the Kaimuqi mafic-ultramafic intrusion.

We calculated the degree of contamination by the country rocks using a two-endmember isotopic mixing model (Fig. 9). The surrounding rock of Kaimuqi mafic-ultramafic intrusion is the Late Triassic biotite monzogranite, and the surrounding rock of the Lata Triassic biotite monzogranite is Proterozoic rocks (Fig. 3). The biotite monzogranite is formed later than the mafic-ultramafic intrusion (Fig. 3). Thus, the Kaimuqi mafic-ultramafic intrusion should be contaminated by the Proterozoic rock. The isotopic compositions of the Hf observed in the studied zircons represent mixtures of different sources, the calculated model ages may represent an average age of the mixed source (Arndt and Goldstein, 1987; Ortega-Obregon et al., 2014). In other words, the two-stage Hf model ages (T(DM2)) provides age information for crust contamination. The zircon two-stage Hf model ages (T(DM2)) from the Kaimuqi websterite are 7 1033–1316 Ma (Table 2). This is consistent with our view that the Kaimuqi mafic-ultramafic intrusion was contaminated by the Proterozoic rocks. The country rocks of the Xiarihamu intrusions are also the Proterozoic rocks. Therefore, we chose the Proterozoic gneiss in the Xiarihamu mine area as one of the endmembers; this rock has 5.35 ppm Hf, an εHf (t = 221 Ma) value of −16.8 and an εHf (*t* = 411 Ma) value of −12.8 (Gan, 2014), calculated from an εHf (t = 915.2 Ma) value of −2.1. We chose the depleted mantle as the other endmember. The Hf content of the depleted mantle (Fig. 9) is 2.05 ppm (Sun and McDonough, 1989), and the εHf (t = 221 Ma) and εHf (t = 411 Ma) values of the depleted mantle are 18.2 and 17.1, respectively, as calculated from (Griffin et al., 2000). Comparing the εHf(t) values of the depleted mantle with those of the Proterozoic gneiss (a potential contaminant) from the Xiarihamu mine area (Gan, 2014) reveals that the Kaimuqi websterite and the Xiarihamu websterite could have experienced up to 26% and 27% contamination, respectively (Fig. 9). Therefore, these samples appear to have experienced similar degrees of crustal contamination. This is consistent with their similar $(^{87}Sr/^{86}Sr)_i$ and εNd(t) composition. However, the Xiarihamu websterite and orthopyroxenite contain significant amounts of sulfides (Table 4), but nearly no sulfides were found in the Kaimuqi websterite. These differences in sulfide abundance likely resulted from factors other than the origin or the degree of crustal contamination.

In Fig. 8, the following differences between the mineralized Xiarihamu mafic-ultramafic intrusion and the non-mineralized Kaimuqi and Binggounan intrusion can be observed: (1) the Kaimuqi and Binggounan olivine contains significantly lower contents of MgO, Fo, and SiO_2 but higher contents of CaO and FeO than the Xiarihamu olivine, and (2) the Kaimuqi clinopyroxene contains higher contents of FeO and CaO than the Xiarihamu clinopyroxene (Fig. 8). The content of major elements in the mineral can reflect the content of the corresponding element in the melt coexisting with it. For example, the relationship between the olivine CaO content and the coexisting melt CaO content, in wt%, follows the following rule (Libourel, 1999):

$$CaO_{Olivine} = 0.0877^{*}(e^{(0.106*CaO_{melt})} - 1).$$

That is, the more Ca-rich the melt, the more Ca-rich the olivine (Libourel, 1999). Therefore, we infer that the Kaimuqi and Binggounan intrusions formed from a magma with higher FeO and CaO contents and lower MgO and SiO_2 contents relative to the Xiarihamu intrusion.

Table 2
Hf isotopic data of zircons from websterite.

No.	$^{176}Hf/^{177}Hf$	2σ	$^{176}Lu/^{177}Hf$	2σ	$^{176}Yb/^{177}Hf$	2σ	Age (Ma)	εHf(t)	$f_{Lu/Hf}$	T(DM1) (Ma)	T(DM2) (Ma)
1	0.282650	0.000028	0.000373	0.000001	0.019267	0.000252	224.3	0.57	−0.99	839	1219
2	0.282620	0.000031	0.000450	0.000003	0.022717	0.000376	222.1	−0.57	−0.99	883	1289
3	0.282685	0.000034	0.000490	0.000019	0.023829	0.000843	221.9	1.70	−0.99	794	1145
4	0.282677	0.000047	0.000647	0.000011	0.034556	0.000886	227.8	1.56	−0.98	807	1158
5	0.282614	0.000029	0.000611	0.000010	0.031671	0.000757	225.5	−0.74	−0.98	895	1302
6	0.282705	0.000040	0.000890	0.000007	0.042285	0.000175	224.0	2.40	−0.97	774	1102
7	0.282667	0.000039	0.000779	0.000001	0.040756	0.000176	222.0	1.03	−0.98	825	1187
8	0.282608	0.000037	0.000301	0.000003	0.015579	0.000313	218.2	−1.05	−0.99	896	1316
9	0.282634	0.000038	0.000155	0.000003	0.007792	0.000083	218.7	−0.12	−1.00	857	1258
10	0.282734	0.000044	0.000826	0.000006	0.042220	0.000506	226.8	3.51	−0.98	731	1033
11	0.282685	0.000045	0.000722	0.000013	0.036888	0.000933	214.7	1.54	−0.98	798	1150
12	0.282645	0.000037	0.000480	0.000004	0.024263	0.000109	213.9	0.13	−0.99	849	1238
13	0.282728	0.000043	0.000672	0.000005	0.033991	0.000328	213.8	3.06	−0.98	736	1052
14	0.282700	0.000042	0.000627	0.000004	0.031435	0.000077	220.6	2.21	−0.98	775	1111
Average	0.282668	0.000038	0.000573	0.000007	0.029089	0.000415	221.0	1.09	−0.98	818	1183

Note: $\varepsilon Hf(t) = \{[(^{176}Hf/^{177}Hf)_S - (^{176}Lu/^{177}Hf)s \times (e^{\lambda t} - 1)]/(^{176}Hf/^{177}Hf)_{CHUR}(t) - 1\} \times 10{,}000$; $(^{176}Hf/^{177}Hf)_{CHUR}(t) = (^{176}Hf/^{177}Hf)_{CHUR}(0) - (^{176}Lu/^{177}Hf)_{CHUR} \times (e^{\lambda t} - 1)$; $T(DM1) = (1/\lambda) \times \ln\{1 + [(^{176}Hf/^{177}Hf)_{DM} - (^{176}Hf/^{177}Hf)s]/[(^{176}Lu/^{177}Hf)_{DM} - (^{176}Lu/^{177}Hf)s]\}$; $T(DM2) = T(DM1) - [T(DM1) - t] \times (f_{CC}-fs)/(fcc-f_{DM})$; $f_{Lu/Hf} = (^{176}Lu/^{177}Hf)_S/(^{176}Lu/^{177}Hf)_{CHUR} - 1$; t is the crystallization age of the zircon, and T(DM1)and T(DM2) are single- and two-stage Hf model ages, respectively; subscript S = analyzed zircon sample, CHUR = chondritic uniform reservoir; DM = depleted mantle; $\lambda = 1.867 \times 10^{-11}$ year^{-1} (Amelin, 2005), decay constant of ^{176}Lu; $(^{176}Hf/^{177}Hf)_{DM} = 0.28325$ (Griffin et al., 2000); $(^{176}Lu/^{177}Hf)_{DM} = 0.0384$ (Griffin et al., 2000); present-day $(^{176}Hf/^{177}Hf)_{CHUR}(0) = 0.282772$ and $(^{176}Lu/^{177}Hf)_{CHUR} = 0.0332$ (Blichert-Toft and Albarède, 1997). $(^{176}Lu/^{177}Hf)_S$ and $(^{176}Hf/^{177}Hf)_S$ are the measured values of samples, f_{CC}, f_S, and f_{DM} are the $f_{Lu/Hf}$ values of the crustal source, sample, and depleted mantle, respectively. $f_{CC} = -0.548$, ($^{176}Lu/^{177}Hf = 0.0093$ in average continental crust; Amelin et al., 1999), and $f_{DM} = 0.157$ ($^{176}Lu/^{177}Hf = 0.0384$; Griffin et al., 2000).

Table 3
Sr-Nd data for the Kaimuqi intrusion and the Xiarihamu Cu-Ni deposit.

Intrusion	Rock type	Age	Rb ($/10^{-6}$)	Sr($/10^{-6}$)	$^{87}Rb/^{86}Sr$	$^{87}Sr/^{86}Sr$	2σ	$(^{87}Sr/^{86}Sr)i$	Data source
Kaimuqi	Websterite	221.1 Ma	59.8	92.7	1.866631	0.715685	0.000006	0.709818	This paper
Kaimuqi	websterite	221.1 Ma	17.6	247	0.206183	0.709696	0.000005	0.709047	This paper
Xiarihamu	Orthopyroxenite	411 Ma	6.5	48.1	0.392319	0.711274	0.000010	0.708974	Zhang et al., 2017
Xiarihamu	Orthopyroxenite	411 Ma	6.5	48	0.392320	0.711294	0.000008	0.708995	Zhang et al., 2017
Xiarihamu	Orthopyroxenite	411 Ma	6.1	24.0	0.734379	0.710730	0.000005	0.706426	Zhang et al., 2017
Intrusion	Rock type	Age	Sm ($/10^{-6}$)	Nd($/10^{-6}$)	$^{147}Sm/^{144}Nd$	$^{143}Nd/^{144}Nd$	2σ	εNd(t)	Data source
Kaimuqi	Websterite	221.1 Ma	1.63	6.10	0.161465	0.512326	0.000005	−5.1	This paper
Kaimuqi	Websterite	221.1 Ma	1.42	6.20	0.138394	0.512345	0.000005	−4.1	This paper
Xiarihamu	Orthopyroxenite	411 Ma	1.36	4.12	0.199555	0.512466	0.000009	−3.5	Zhang et al., 2017
Xiarihamu	Orthopyroxenite	411 Ma	1.36	4.12	0.199554	0.512442	0.000007	−4.0	Zhang et al., 2017
Xiarihamu	Orthopyroxenite	411 Ma	0.50	1.67	0.180997	0.512433	0.000009	−3.2	Zhang et al., 2017

Xiarihamu Age data from Li et al., 2015.

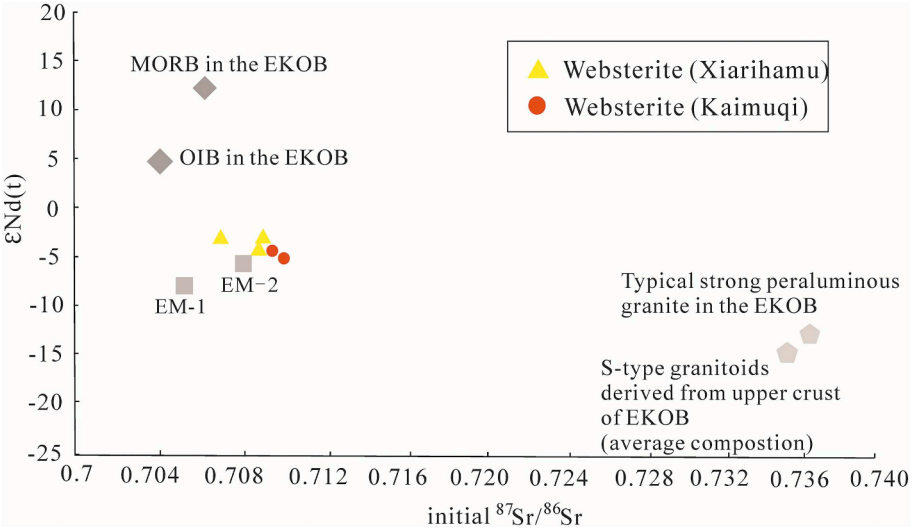

Fig. 7. εNd(t)–($^{87}Sr/^{86}Sr$)i values of the Xiarihamu orthopyroxenite and Kaimuqi websterite.
The Xiarihamu Sr-Nd isotopic values are from Zhang et al. (2017).
EM-1 = Enriched Mantle-1, and EM-2 = Enriched Mantle-2. The Sr-Nd isotope areas of these two mantle sources are from Hofmann (2007). MORB and Oceanic-island basalt (OIB) area of the EKOB are from Guo et al. (2007). MORB and Oceanic-island basalt (OIB) area of the EKOB are from Guo et al. (2007). The field of Typical strong peraaluminous granite in the EKOB is from Ba et al. (2012). S-type granitoids derived from upper crust of EKOB is from B. Liu et al. (2017).

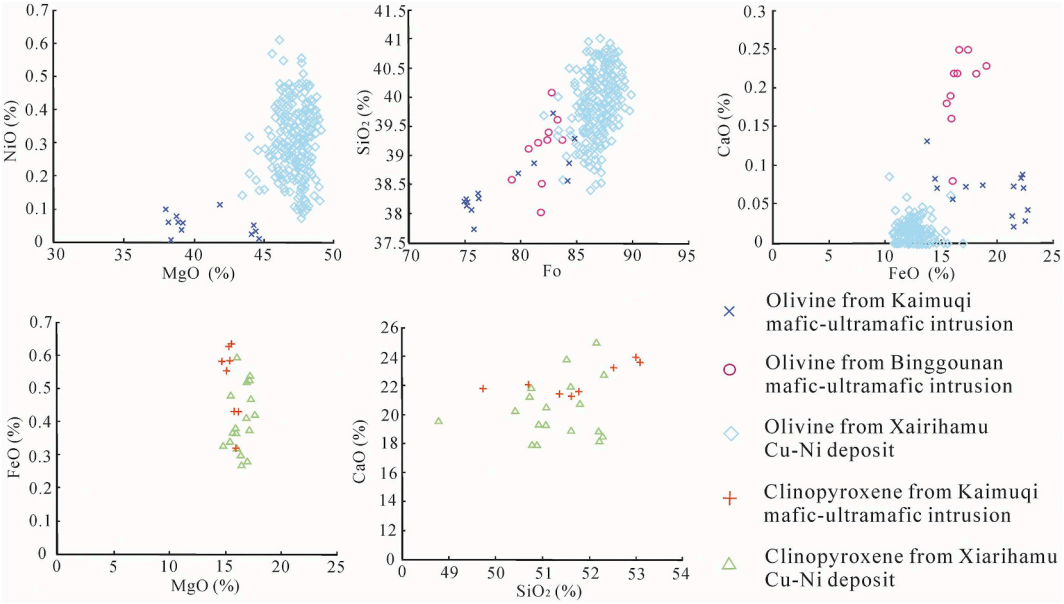

Fig. 8. Comparison of the olivine and clinopyroxene compositions from the Xiarihamu and Kaimuqi mafic-ultramafic intrusions
The Xiarihamu olivine data are from Ling (2014), Wang (2014), Li et al. (2015), the Binggounan olivine data are from Wang (2014), and the Xiarihamu clinopyroxene data are from Ling (2014) and Wang (2014).

Table 4
Geological characteristics of mafic-ultramafic intrusions in East Kunlun.

Intrusion	Age	Rock type	Lithofacies containing ore	Ore structure	Whole rock m/f	Resources
Xiarihamu 1	406.1 ± 2.7 Ma; 411.6 ± 2.4 Ma (websterite Age)	Gabbro, websterite, lherzolite, orthopyroxenite, websterite, harzburgite, dunite	Websterite, orthopyroxenite, dunite	Massive; patchy sulfide; heavily disseminated sulfide; sparse disseminated sulfide; vein sulfide	2.06–6.3	(Ling, 2014; Li et al., 2015; Song et al., 2016; Liu et al., 2018)
Binggounan	427.4 ± 7.3 Ma	Troctolite, gabbro, diorite	None	None	2.5–2.9	(Wang, 2014; Yan et al., 2016)
Shitoukengde	423.5 ± 3.2 Ma (Gabbro Zircon U-Pb age from Zhou (2016)); 333.9 ± 4.2 Ma (olivine-websterite zircon U-Pb age from Zhang et al. (2018)); 422.1 ± 1.5 Ma (olivine-websterite U-Pb age from Li et al. (2018)).	Gabbro, olivine-gabbro, clinopyroxenite, websterite, orthopyroxenite, wehrlite, lherzolite, harzburgite, dunite	Websterite	Massive; patchy sulfide; heavily disseminated sulfide; sparse disseminated sulfide; vein sulfide	3.61–5.55	(Zhou, 2016)
Kaimuqi	221.0 ± 2.1 Ma	Plagioclase-wehrlite, websterite (Cpx 75%, Opx 20%), gabbro	None	None		This paper
Xiaojianshan	227.8 ± 0.9 Ma (Gabbro LA-MC-ICP-MS zircon U-Pb age)	Olivine-gabbro, gabbro	None	None	1.5–2.9	(Ao et al., 2015)

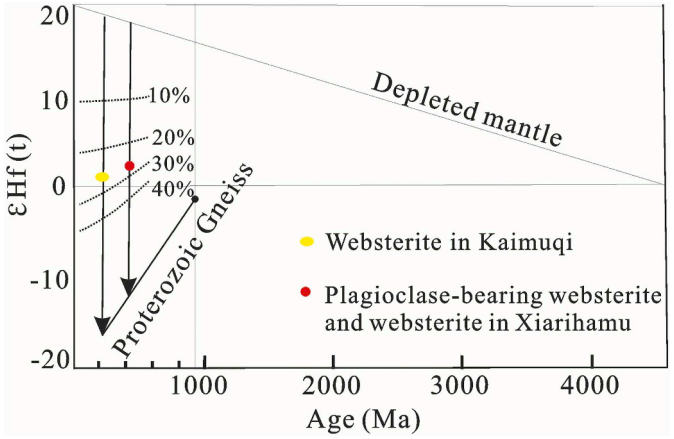

Fig. 9. Quantitative simulation of the degree of contamination with Proterozoic gneiss for the Kaimuqi websterite and the Xiarihamu websterite.
The Xiarihamu Hf isotopic data are from Li et al. (2015).

Magmatic sulfide deposits are formed by the segregation of sulfides from mantle-derived mafic-ultramafic magmas (Naldrett, 2004). The distribution coefficients between sulfides and silicates ($D_{Sul/Sil}$) range from 4×10^5 to $2–3 \times 10^6$ for platinum group elements (PGEs) (Mungall and Brenan, 2014). Li and Audétat (2015) suggested that the $D_{Sul/Sil}$ of Ni is 2300 to 18,000, and Cu is 800 to 4600; Patten et al. (2013) suggested that $D_{Sul/Sil}$ of Ni is 776, and Cu is 1334. Therefore, Cu, Ni, and PGEs are highly compatible in sulfides. The occurrence of sulfides in silicate melts requires sulfide saturation in the magma system, and the sulfur content at sulfide saturation (SCSS) is greatly influenced by the composition of the magma (Liu et al., 2007; Li and Ripley, 2009). Li and Ripley (2009) presented an empirical equation with which to calculate the SCSS based on available experimental results. The SCSS conforms to Eq. (1), where P is in kbar, T is in Kelvin, X is the mole fraction, and Xi is the mole fraction of oxide i in the melt:

$$\ln X_S = -1.76 - 0.474\,(10^4/T) - 0.021P + 5.559XFeO + 2.565XTiO_2 + 2.709\,XCaO - 3.192\,XSiO_2 + 3.049\,XH_2O \quad (1)$$

Generally, the SCSS is positively correlated with the contents of FeO, TiO_2, and CaO and negatively correlated with SiO_2 (Wendlandt, 1982; Mavrogenes and O'Neill, 1999; Liu et al., 2007; Li and Ripley, 2009). The Kaimuqi and Binggounan intrusions formed from a melt with higher FeO and CaO contents and a lower SiO_2 content. This melt thus required a higher sulfur content to achieve sulfide saturation. This characteristic most likely hindered mineralization in the Kaimuqi and Binggounan mafic-ultramafic intrusions.

In Table 4, the following differences between the mineralized mafic-ultramafic intrusions and the non-mineralized mafic-ultramafic intrusions can be observed: (1) the mineralized intrusions contain dunite, lherzolite, harzburgite and orthopyroxenite; and (2) the range of m/f values ($(Mg + Ni)/(Fe^{2+} + Fe^{3+} + Mn)$) is broader ($m/f_{max}$-$m/f_{min} > 2.5$) and the m/f values are higher ($m/f_{max} > 5.5$) in the mineralized intrusions than in the non-mineralized intrusions. We used the rhyolite-MELTS program (http://melts.ofm-research.org/macosx.html) developed by Gualda et al. (2012) and Ghiorso and Gualda (2015) to estimate the relationship between the fractional crystallization of different minerals and the SCSS. We assumed the following composition of the parental magma: MgO = 14.48, FeO = 6.38, Fe_2O_3 = 0.84, SiO_2 = 50.20, Al_2O_3 = 13.77, CaO = 9.6, K_2O = 0.28, MnO = 0.11, Na_2O = 2.14, Cr_2O_3 = 0.06, P_2O_5 = 0.03, NiO = 0.05, TiO_2 = 0.59 and LOI = 1.47. We used this liquid composition of the parental magma, a fixed $logfO_2$ of FMQ +0 and a fixed pressure of 1 kbar in the rhyolite-MELTS program to simulate fractional crystallization between 1200 °C (the primary temperature) and 900 °C (Fig. 10). Fig. 10 shows that the sole crystalline phase that forms

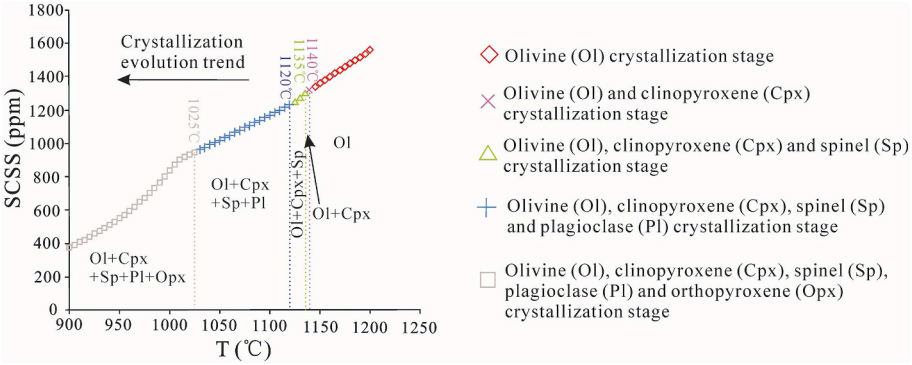

Fig. 10. Model of the variation in the sulfur contents at sulfide saturation (SCSS) during fractional crystallization. The modeling details were provided in the text.

between 1200 °C and 1145 °C is olivine and that clinopyroxene, spinel, plagioclase, and orthopyroxene crystallize at 1140 °C, 1135 °C, 1120 °C, and 1025 °C, respectively. The crystallization process leads to a drop in the SCSS (Fig. 10). The mineralized mafic-ultramafic intrusions exhibit both a broader range of m/f values and higher m/f values than the non-mineralized intrusions, which means that the mineralized intrusions experienced a long process of crystallization differentiation. This process is probably responsible for the Cu-Ni mineralization in the Xiarihamu and Shitoukengde intrusions.

Clinopyroxene (Ca (Mg, Fe^{2+}, Fe^{3+}, Ti, Al) $[(Si,Al)_2O_6]$) is a calcium-rich mineral. On the contrary, almost no calcium is contained in the orthopyroxene ($(Mg, Fe^{2+})_2[Si_2O_6]$). Therefore, an intrusion contains more clinopyroxene indicates that its magma contains more calcium. The magma with higher calcium content will need a higher sulfur content to achieve sulfide saturation (Liu et al., 2017). Thus, the pyroxene in an intrusion is mainly clinopyroxene is a bad news for the Cu-Ni mineralization. The Xiarihamu and Shitoukengde mafic-ultramafic intrusions contain harzburgite, orthopyroxenite, and websterite, indicating that the pyroxene in these intrusions is mainly orthopyroxene. This is probably one of the reasons why the Xiarihamu and Shitoukengde intrusions contain Cu-Ni mineralization. Although websterite occurred in the Kaimuqi intrusion, the clinopyroxene and orthopyroxene content in the websterite is 75% and 20%, respectively (Fig. 4b), and the peridotite lithofacies is wehrlite. Therefore, the orthopyroxene is rare in the Kaimuqi mafic-ultramafic intrusions, and the pyroxene is mainly the clinopyroxene. Thus, the Kaimuqi mafic-ultramafic intrusions may not have had the potential to form Cu-Ni ore deposits.

7. Conclusions

The U-Pb age of websterite in the Kaimuqi mafic-ultramafic intrusion is 221.1 ± 2.3 Ma. None the Middle-Late Triassic mafic-ultramafic intrusions in the EKOB have Cu-Ni mineralization. Compared to the olivine in the Xiarihamu giant Cu-Ni deposit, the Kaimuqi olivine contains significantly lower contents of MgO, NiO, Fo, and SiO_2 but higher contents of CaO and FeO. Furthermore, the Kaimuqi clinopyroxene also contains higher FeO and CaO contents than the Xiarihamu clinopyroxene. Therefore, we infer that the Kaimuqi intrusion formed from a melt with higher FeO and CaO contents and a lower SiO_2 content than the Xiarihamu intrusion. This melt required more sulfur to achieve sulfide saturation, which probably hindered mineralization in the Kaimuqi mafic-ultramafic intrusion. Mafic-ultramafic intrusions that contain more orthopyroxene than clinopyroxene are more likely to form Cu-Ni mineralization, as an intrusion contains more clinopyroxene indicate that its magma contains more calcium. The magma with higher calcium content will need a higher sulfur content to achieve sulfide saturation. Orthopyroxene is rare in the Kaimuqi mafic-ultramafic intrusion, and the pyroxene is mainly the clinopyroxene, which most likely indicate that the Kaimuqi mafic-ultramafic intrusion may not have had the potential to form Cu-Ni ore deposits.

The mafic-ultramafic intrusions in the EKOB that have Cu-Ni mineralization potential share the following characteristics: (1) the Late Silurian-Early Devonian mafic-ultramafic intrusions may be better suited for Cu-Ni mineralization; (2) mineralized mafic-ultramafic complexes have a broader range of m/f values (m/f_{max}-m/f_{min} > 2.5) and higher m/f values (m/f_{max} > 5.5); (3) the pyroxene in the intrusion is mainly orthopyroxene; (4) the olivine in mineralized intrusions features high MgO (> 45%), NiO, Fo (> 85%), and SiO_2 contents and low CaO (< 0.05%) and FeO (< 15%) contents; and (5) the clinopyroxene in mineralized intrusions contains low contents of FeO and CaO (< 20%). These features provide some enlightenment to the exploration of Cu-Ni deposits in mafic-ultramafic intrusions, especially for the geological exploration bureaus or companies, which do not have the budget for large numbers of geological dating, isotopes, major elements, and platinum group elements during the exploration evaluation process in the current global mining recession situation.

Supplementary data to this article can be found online at https://doi.org/10.1016/j.gexplo.2018.12.002.

Acknowledgments

We are grateful to the Associate Editor and the anonymous reviewers for their great help in improving this manuscript. We appreciate the great help in Melts software from Dr. Juan Duan from Chang'an University. This study was financially supported by the Special Fund for Land and Resources Scientific Research of Public Interest (201511020), China Geological Survey Project (DD20160013), the State Scholarship Fund ([2016]3035-201608610016) from the China Scholarship Council, the China Postdoctoral Science Foundation (2015M582762XB), the Shaanxi Province Postdoctoral Science Foundation (2017BSHQYXMZZ06), the Natural Science Foundation of Shaanxi Province (2017JM4002), and Natural Science Foundation of China (41873053), 1:50000 geological survey of J46E020013, J46E021013, and J46E022013 in the Lalinggaolihe area of Golmud in Qinghai (121201011000150005-19).

References

Amelin, Y., 2005. Meteorite phosphates show constant ^{176}Lu decay rate since 4557 million years ago. Science 310, 839–841.
Amelin, Y., Lee, D.C., Halliday, A.N., Pidgeon, R.T., 1999. Nature of the Earth's earliest crust from hafnium isotopes in single detrital zircons. Nature 399, 252.
Ao, C., 2014. Study on Geological Characteristics and Genesis of Xiarihamu Nickel Deposit, Qinghai Province. Jilin University Master Thesis. pp. 1–86 (in Chinese with English abs.).
Ao, C., Sun, F., Li, B., Wang, G., Li, L., Li, S., Zhao, J., 2015. U-Pb dating, geochemistry and tectonic implications of Xiaojianshan gabbro in Qimantage mountain, Eastern Kunlun orogenic belt. Geotecton. Metallog. 39, 1176–1184 (in Chinese with English abs.).
Arndt, N.T., Goldstein, S.L., 1987. Use and abuse of crust-formation ages. Geology 15, 893–895.
Ba, J., Chen, N.S., Wang, Q.Y., Wang, X.Y., Zhang, L., Wang, S.Q., 2012. Nd–Sr–Pb isotopic compositions of cordierite granite on southern margin of the Qaidam Block, NW

China, and constraints on its petrogenesis, tectonic affinity of source region and tectonic implications. Earth Sci. J. China Univ. Geosci. 80–92 (in Chinese with English abstract).
Barnes, S.J., Lightfoot, P.C., 2005. Formation of magmatic nickel sulfide ore deposits and processes affecting their copper and platinum-group contents. Econ. Geol. 100th Anniversary, 173–213.
Barnes, S.J., Naldrett, A.J., 1985. Geochemistry of the JM (Howland) reef of the stillwater complex, minneapolis adit area; I, sulfide chemistry and sulfide-olivine equilibrium. Econ. Geol. 39 (80), 627–645.
Barnes, S.J., Couture, J.F., Sawyer, E.W., Bouchaib, C., 1993. Nickelcopper occurrences in the Belleterre-Angliers Belt of the Pontiac Subprovince and the use of Cu-Pd ratios in interpreting platinum-group element distributions. Econ. Geol. 88, 1402–1418.
Basu, A.R., Wang, J.W., Huang, W., Xie, G., Mitsunobu, T., 1991. Major element, REE, and Pb, Nd and Sr isotopic geochemistry of Cenozoic volcanic rocks of eastern China: implications for their origin from suboceanic-type mantle reservoirs. Earth Planet. Sci. Lett. 105, 149–169.
Blichert-Toft, J., Albarède, F., 1997. The Lu-Hf isotope geochemistry of chondrites and the evolution of the mantle-crust system. Earth Planet. Sci. Lett. 148, 243–258.
Chen, L., Sun, Y., Pei, X., Feng, T., Zhang, G., 2003. Comparison of eastern Paleo-Tethyan ophiolites and its geodynamic significance: evidence from Dur'ngoi ophiolite. Sci. China Earth Sci. 33, 1136–1142.
Chen, G., Pei, X., Li, R., Li, Z., Pei, L., Liu, Z., Chen, Y., Liu, C., Gao, J., Wei, F., 2013. Geochronology and genesis of the Helegang Xilikete granitic plutons from the southern margin of the eastern East Kunlun orogenic belt and their tectonic significance. Acta Geol. Sin. 87, 1525–1541 (in Chinese with English abs.).
Ding, S., Huang, H., Niu, Y., Zhao, Z., Yu, X., Mo, X., 2011. Geochemistry, geochronology and petrogenesis of East Kunlun high Nb-Ta rhyolites. Acta Petrol. Sin. 27, 3603–3614 (in Chinese with English abs.).
Ding, Q.F., Jiang, S.Y., Sun, F.Y., 2014. Zircon U–Pb geochronology, geochemical and Sr–Nd–Hf isotopic compositions of the Triassic granite and diorite dikes from the Wulonggou mining area in the Eastern Kunlun Orogen, NW China: petrogenesis and tectonic implications. Lithos 205, 266–283.
Duan, J., Li, C., Qian, Z., Jiao, J., Ripley, E.M., Feng, Y., 2016. Multiple S isotopes, zircon Hf isotopes, whole-rock Sr-Nd isotopes, and spatial variations of PGE tenors in the Jinchuan Ni-Cu-PGE deposit, NW China. Mineral. Deposita 51 (4), 557–574.
Feng, C., Wang, S., Li, G., Ma, S., Li, D., 2012. Middle to Late Triassic granitoids in the Qimantage area, Qinghai Province, China: Chronology, geochemistry and metallogenic significances. Acta Geol. Sin. 28, 665–678 (in Chinese with English abs.).
Gan, C., 2014. Petrology, Geochemistry, U-Pb Dating and Hf Isotopic Composition of Zircons in Igneous Rocks from East Kunlun Orogen, Qinghai. A Dissertation Submitted to the China University of Geosciences for Master Degree. pp. 1–75 (in Chinese with English abs.).
Ghiorso, M.S., Gualda, G.A.R., 2015. An H_2O–CO_2 mixed fluid saturation model compatible with rhyolite-MELTS. Contrib. Mineral. Petrol. 169, 53.
Griffin, W.L., Pearson, N.J., Belousova, E., Jackson, S.E., Achterbergh, E.V., O'Reilly, S.Y., Shee, S.R., 2000. The Hf isotope composition of cratonic mantle: LAM-MC-ICPMS analysis of zircon megacrysts in kimberlites. Geochim. Cosmochim. Acta 64, 133–147.
Gualda, G.A.R., Ghiorso, M.S., Lemons, R.V., Carley, T.L., 2012. Rhyolite-MELTS: a modified calibration of MELTS optimized for silica-rich, fluid-bearing magmatic systems. J. Petrol. 53, 875–890.
GUG (China University of Geosciences (Wuhan)), 2003. 1: 250,000 Alake Hu Regional Geological Survey Report. pp. 1–350 (in Chinese).
Guo, A.L., Zhang, G.W., Sun, Y.G., Cheng, S.Y., Qiang, J., 2007. Sr–Nd–Pb isotopic geochemistry of late-Paleozoic mafic volcanic rocks in the surrounding areas of the Gonghe basin, Qinghai province and geological implications. Acta Geol. Sin. 23, 747–754 (in Chinese with English abs.).
Hiebert, R.S., Bekker, A., Wing, B.A., Rouxel, O.J., 2013. The role of paragneiss assimilation in the origin of the Voisey's Bay Ni-Cu sulfide deposit, Labrador: multiple S and Fe isotope evidence. Econ. Geol. 108 (6), 1459–1469.
Hofmann, A.W., 2007. Sampling mantle heterogeneity through oceanic basalts: isotopes and trace elements. Treatise Geochem. 2, 1–44.
Hou, K.J., Li, Y.H., Zou, T.R., Qu, X.M., Shi, Y.R., Xie, G.Q., 2007. Laser ablation-MC-ICP-MS technique for Hf isotope microanalysis of zircon and its geological applications. Acta Petrol. Sin. 23, 2595–2604 (in Chinese with English abs.).
Hu, Z., Gao, S., Liu, Y., Hu, S., Chen, H., Yuan, H., 2008. Signal enhancement in laser ablation ICP-MS by addition of nitrogen in the central channel gas. J. Anal. At. Spectrom. 23, 1093–1101.
Hu, Z., Liu, Y., Gao, S., Xiao, S., Zhao, L., Günther, D., Li, M., Zhang, W., Zong, K., 2012. A "wire" signal smoothing device for laser ablation inductively coupled plasma mass spectrometry analysis. Spectrochim. Acta B 78, 50–57.
Hu, Y., Niu, Y., Li, J., Ye, L., Kong, J., Chen, S., Zhang, Y., Zhang, G., 2016. Petrogenesis and tectonic significance of the late Triassic mafic dikes and felsic volcanic rocks in the East Kunlun Orogenic Belt, Northern Tibet Plateau. Lithos 245, 205–222.
Huang, J., Chen, G.M., Chen, B.W., 1984. Preliminary analysis of the Tethys-Himalayan tectonic domain: Huang, Jiqing, Guoming Chen and Bingwei Chen, 1984. Acta Geol. Sin. 58, 1–17 ((In Chinese, English abstract.). Deep Sea Research Part B: Oceanographic Literature Review 31, 876).
Jackson, S.E., Pearson, N.J., Griffin, W.L., Belousova, E.A., 2004. The application of laser ablation-inductively coupled plasma-mass spectrometry to in situ U–Pb zircon geochronology. Chem. Geol. 211, 47–69.
Jiang, C., Yang, J., Feng, B., Zhu, Z., Zhao, M., Chai, Y., Shi, X., Wang, H., Hu, J., 1992. Opening-Closing Tectonics of Kunlun Mountains. Geological Publishing House, Beijing, pp. 1–224 (in Chinese).
Jiang, C.Y., Lu, D.R., Bai, K.Y., Zhang, P.B., Ye, S.F., Feng, J.X., Chen, W.G., 2005. Metasomatism products of continental lithosphere mantle - Roseite deposits, Qieganbulake. Acta Petrol. Sin. 21, 201–210 (in Chinese with English abs.).
Jiang, C., Ling, J., Zhou, W., Du, W., Wang, Z., Fan, Y., Song, Y., Song, Z., 2015. Petrogenesis of the Xiarihamu Ni bearing layered mafic-ultramafic intrusion, East Kunlun: Implications for its extensional island arc environment. Acta Petrol. Sin. 31 (4), 1117–1136.
Lacono-Marziano, G., Ferraina, C., Gaillard, F., Carlo, I.D., Arndt, N.T., 2017. Assimilation of sulfate and carbonaceous rocks: experimental study, thermodynamic modeling and application to the Noril'sk-Talnakh region (Russia). Ore Geol. Rev. 90, 399–413.
Lehmann, J., Arndt, N., Windley, B., Zhou, M.F., Wang, C.Y., Harris, C., 2007. Field Relationships and Geochemical Constraints on the Emplacement of the Jinchuan Intrusion and its Ni-Cu-PGE Sulfide Deposit, Gansu, China. Econ. Geol. 102, 75–94.
Li, Y., Audétat, A., 2015. Effects of temperature, silicate melt composition, and oxygen fugacity on the partitioning of V, Mn, Co, Ni, Cu, Zn, As, Mo, Ag, Sn, Sb, W, Au, Pb, and Bi between sulfide phases and silicate melt. Geochim. Cosmochim. Acta 162, 25–45.
Li, C., Ripley, E.M., 2009. Sulfur contents at sulfide-liquid or anhydrite saturation in silicate melts: empirical equations and example applications. Econ. Geol. 104, 405–412.
Li, C., Ripley, E.M., 2011. The giant Jinchuan Ni-Cu-(PGE) deposit; tectonic setting, magma evolution, ore genesis, and exploration implications. Rev. Econ. Geol. 17, 163–180.
Li, H.K., Lu, S.N., Xiang, Z.Q., Zhou, H.Y., Guo, H., Song, B., Zheng, J.K., Gu, Y., 2006. SHRIMP U-Pb zircon age of the granulite from the Qingshuiquan area, Central Eastern Kunlun Suture Zone. Earth Sci. Front. 13, 311–321 (in Chinese with English abs.).
Li, S.J., Sun, F.Y., Gao, Y.W., Zhao, J.W., Li, L.S., Yang, Q., 2012. The theoretical guidance and the practice of small intrusions forming large deposits - The enlightenment and significance for searching breakthrough of Cu-Ni sulfide deposit in Xiarihamu, East Kunlun, Qinghai. Northwest. Geol. 45 (4), 185–191 (in Chinese with English abs.).
Li, J., Jia, Q., Wei, D., Li, Y., Kong, H., Norbu, N., Yang, B., 2014. LA-ICP-MS Zircon Dating and Geochemical Characteristics of Quartz Diorite in Asiha Gold Deposit in East Segment of the Eastern Kunlun. J. Jilin Univ. (Earth Sci. Ed.) 44, 1188–1199 (in Chinese with English abs.).
Li, C., Zhang, Z., Li, W., Wang, Y., Sun, T., Ripley, E.M., 2015. Geochronology, petrology and Hf–S isotope geochemistry of the newly-discovered Xiarihamu magmatic Ni–Cu sulfide deposit in the Qinghai–Tibet plateau, western China. Lithos 224–240.
Li, L., Sun, F.Y., Li, B.L., Li, S.J., Chen, G.J., Wang, W., Yan, J.M., Zhao, T.F., Dong, J., Zhang, D.X., 2018. Geochronology, geochemistry and Sr-Nd-Pb-Hf isotopes of no. I complex from the Shitoukengde Ni–Cu sulfide deposit in the Eastern Kunlun Orogen, Western China: implications for the magmatic source, geodynamic setting and genesis. Acta Geol. Sin. (Engl. Ed.) 92, 106–126.
Libourel, G., 1999. Systematics of calcium partitioning between olivine and silicate melt: implications for melt structure and calcium content of magmatic olivines. Contrib. Mineral. Petrol. 136, 63–80.
Lightfoot, P.C., Milkereit, B., 2007. Advances in Ni-Cu-PGE sulphide deposit models and implications for exploration technologies. Proc. Explor. 629–646.
Lightfoot, P., Naldrett, A., 1999. Geological and geochemical relationships in the Voisey's Bay intrusion, Nain plutonic suite, Labrador, Canada. Geol. Assoc. Canada Short Course Notes 13, 1–30.
Lightfoot, P.C., Keays, R.R., Evans-Lamswood, D., Wheeler, R., 2012. S saturation history of Nain Plutonic Suite mafic intrusions: origin of the Voisey's Bay Ni–Cu–Co sulfide deposit, Labrador, Canada. Mineral. Deposita 47 (1), 23–50.
Ling, J.L., 2014. Metallogenesis of Nickel Deposits in Eastern Kunlun Orogenic Belt, Qinghai Province. Doctoral Dissertation for Chang'an University, Xi'an. pp. 1–214 (in Chinese with English abs.).
Liu, B., Ma, C.Q., Zhang, J.Y., Xiong, F.H., Huang, J., Jiang, H.A., 2012. Petrogenesis of Early Devonian intrusive rocks in the east part of Eastern Kunlun Orogen and implication for Early Palaeozoic orogenic processes. Acta Petrol. Sin. 28, 1785–1807 (in Chinese with English abs.).
Liu, B., Ma, C.Q., Jiang, H.A., Guo, P., Zhang, J.Y., Xiong, F.H., 2013a. Early Paleozoic tectonic transition from ocean subduction to collisional orogeny in the Eastern Kunlun region: evidence from Huxiaoqin Mafic rocks. Acta Petrol. Sin. 29, 2093–2106 (in Chinese with English abs.).
Liu, B., Ma, C.Q., Pan, G., Zhang, J.Y., Xiong, F.H., Jian, H., Jiang, H.A., 2013b. Discovery of the Middle Devonian A-type Granite from the Eastern Kunlun Orogen and Its Tectonic Implications. Earth Sci. J. China Univ. Geosci. 38, 947–962 (in Chinese with English abs.).
Liu, B., Ma, C.Q., Zhang, J.Y., Xiong, F.H., Huang, J., Jiang, H.A., 2014. ^{40}Ar–^{39}Ar age and geochemistry of subduction-related mafic dikes in northern Tibet, China: petrogenesis and tectonic implications. Int. Geol. Rev. 56, 57–73.
Liu, B., Ma, C.Q., Huang, J., Wang, L.X., Zhao, S.Q., Yan, R., Sun, Y., Xiong, F.H., 2017. Petrogenesis and tectonic implications of Upper Triassic appinite dykes in the East Kunlun orogenic belt, northern Tibetan Plateau. Lithos 284, 766–778.
Liu, Y., Samaha, N.T., Baker, D.R., 2007. Sulfur concentration at sulfide saturation (SCSS) in magmatic silicate melts. Geochim. Cosmochim. Acta 71, 1783–1799.
Liu, Y., Zong, K., Kelemen, P.B., Gao, S., 2008. Geochemistry and magmatic history of eclogites and ultramafic rocks from the Chinese continental scientific drill hole: subduction and ultrahigh-pressure metamorphism of lower crustal cumulates. Chem. Geol. 247, 133–153.
Liu, Y., Gao, S., Hu, Z., Gao, C., Zong, K., Wang, D., 2010. Continental and oceanic crust recycling-induced melt–peridotite interactions in the trans-North China Orogen: U–Pb dating, Hf isotopes and trace elements in zircons from mantle xenoliths. J. Petrol. 51, 537–571.
Liu, Y.G., Lü, X.B., Wu, C.M., Hu, X.G., Duan, Z.P., Deng, G., Wang, H., Zhu, X., Zeng, H.D., Wang, P., 2016. The migration of Tarim plume magma toward the northeast in Early Permian and its significance for the exploration of PGE-Cu-Ni magmatic sulfide

deposits in Xinjiang, NW China: as suggested by Sr-Nd-Hf isotopes, sedimentology and geophysical data. Ore Geol. Rev. 72, 538–545.
Liu, Y.G., Li, W.Y., Lü, X.B., Liu, Y.R., Ruan, B.X., Liu, X., 2017. Sulfide saturation mechanism of the Poyi magmatic Cu-Ni sulfide deposit in Beishan, Xinjiang, Northwest China. Ore Geol. Rev. 91, 419–431.
Liu, Y.G., Li, W.Y., Jia, Q.Z., Zhang, Z.W., Wang, Z.A., Zhang, Z.B., Zhang, J.W., Qian, B., 2018. The dynamic sulfide saturation process and a possible slab break-off model for the giant Xiarihamu magmatic nickel ore deposit in the East Kunlun Orogenic Belt, Northern Qinghai-Tibet Plateau, China. Econ. Geol. 113, 1383–1417.
Ludwig, K.R., 2003. User's manual for Isoplot 3.00: a geochronological toolkit for Microsoft Excel. Kenneth R. Ludwig.
Luo, Z., Ke, S., Cao, Y., Deng, J., Chen, H., 2002. Late Indosinian mantle-derived magmatism in the East Kunlun. Geol. Bull. China 21, 292–297 (in Chinese with English abs.).
Luo, M.F., Mo, X.X., Yu, X.H., Li, X.W., Huang, X.F., Yu, J.C., 2014. Zircon LA-ICP-MS U-Pb age dating, petrogenesis and tectonic implications of the Late Triassic granites from the Xiangride area, East Kunlun. Acta Petrol. Sin. 30, 3229–3241 (in Chinese with English abs.).
Manor, M.J., Scoates, J.S., Nixon, G.T., Ames, D.E., 2014. Platinum-group mineralogy of the Giant Mascot Ni-Cu-PGE deposit, Hope, BC. Mineral Explor. 141–156.
Manor, M.J., Scoates, J.S., Nixon, G.T., Ames, D.E., 2016. The giant Mascot Ni-Cu-PGE deposit, British Columbia: mineralized conduits in a convergent margin tectonic setting. Econ. Geol. 111 (1), 57–87.
Mao, J.W., Pirajno, F., Zhang, Z.H., Chai, F.M., Wu, H., Chen, S.P., Cheng, L.S., Yang, J.M., Zhang, C.Q., 2008. A review of the Cu–Ni sulphide deposits in the Chinese Tianshan and Altay orogens (Xinjiang Autonomous Region, NW China): principal characteristics and ore-forming processes. J. Asian Earth Sci. 32 (2), 184–203.
Mavrogenes, J.A., O'Neill, H.S.C., 1999. The relative effects of pressure, temperature and oxygen fugacity on the solubility of sulfide in mafic magmas. Geochim. Cosmochim. Acta 63, 1173–1180.
Meng, F., Zhang, J., Cui, M., 2013. Discovery of Early Paleozoic eclogite from the East Kunlun, Western China and its tectonic significance. Gondwana Res. 23, 825–836.
Meng, E., Liu, F.L., Liu, P.H., Liu, C.H., Yang, H., Wang, F., Shi, J.R., Cai, J., 2014. Petrogenesis and tectonic significance of Paleoproterozoic meta-mafic rocks from central Liaodong Peninsula, Northeast China: evidence from zircon U-Pb dating and in situ Lu-Hf isotopes, and whole-rock geochemistry. Precambrian Res. 247, 92–109.
Mo, X.X., Luo, Z.H., Deng, J.F., Yu, X.H., Liu, C.D., Yuan, W.M., Liu, Y.H., 2007. Granitoids and Crustal Growth in the East-Kunlun Orogenic Belt. Geol. J. China Univ. 13, 403–414 (in Chinese with English abs.).
Moller, A., O'Brien, P.J., Kennedy, A., Kroner, A., 2003. Linking growth episodes of zircon and metamorphic textures to zircon chemistry: an example from the ultrahigh-temperature granulites of Rogaland (SW Norway). Geol. Soc. Lond. Spec. Publ. 220, 65–81.
Mungall, J.E., Brenan, J.M., 2014. Partitioning of platinum-group elements and Au between sulfide liquid and basalt and the origins of mantle-crust fractionation of the chalcophile elements. Geochim. Cosmochim. Acta 125, 265–289.
Naldrett, A.J., 2004. Magmatic Sulfide Deposits: Geology, Geochemistry and Exploration. Springer, pp. 1–728.
Naldrett, A., 2011. Fundamentals of magmatic sulfide deposits. Rev. Econ. Geol. 17, 1–50.
Naldrett, A.J., Singh, J., Krstic, S., Li, C., 2000. The mineralogy of the Voisey's Bay Ni-Cu-Co deposit, Northern Labrador, Canada: influence of oxidation state on textures and mineral compositions. Econ. Geol. 95 (4), 889–900.
National Standard of the People's Republic of China, 1998. General Specification of X-ray EDS Quantitative Analysis for EPMA and SEM.
Nixon, G.T., 2002. Use of Spinel in Mineral Exploration: The Enigmatic Giant Mascot Ni-Cu-PGE Deposit: Possible Ties to Wrangellia and Metallogenic Significance. British Columbia Geological Survey, pp. 115–128.
No. 5 GMSQH (No. 5 Geological and Mineral Survey Institute of Qinghai Province), 2014. Investigation Report on HS26 Abnormal Zone in the Xiarihamu Cu-Ni Mining Area in Golmud City, Qinghai Province. pp. 1–189 (in Chinese).
Ortega-Obregon, C., Solari, L., Gomez-Tuena, A., Elias-Herrera, M., Ortega-Gutierrez, F., Macias-Romo, C., 2014. Permian-Carboniferous arc magmatism in southern Mexico: U-Pb dating, trace element and Hf isotopic evidence on zircons of earliest subduction beneath the western margin of Gondwana. Int. J. Earth Sci. 103, 1287–1300.
Page, N.J., 1971. Comments on the role of oxygen fugacity in the formation of immiscible sulfide liquids in the H chromitite zone of the Stillwater complex, Montana. Econ. Geol. 66 (4), 607–610.
Patten, C., Barnes, S.J., Mathez, E.A., Jenner, F.E., 2013. Partition coefficients of chalcophile elements between sulfide and silicate melts and the early crystallization history of sulfide liquid: LA-ICP-MS analysis of MORB sulfide droplets. Chem. Geol. 358, 170–188.
Peng, B., Sun, F., Li, B., Wang, G., Li, S., Zhao, T., Li, L., Zhi, Y., 2016. The geochemistry and geochronology of the Xiarihamu II mafic–ultramafic complex, Eastern Kunlun, Qinghai Province, China: implications for the genesis of magmatic Ni–Cu sulfide deposits. Ore Geol. Rev. 73, 13–28.
QGS (Qinghai Geological Survey), 2012. 1:50,000 Investigation on Geological and Mineral Resources in Lalingzaohuo, Qinghai. pp. 1–142 (in Chinese).
Raedeke, L.D., Vian, R.W., 1986. A three-dimensional view of mineralization in the Stillwater JM Reef. Econ. Geol. 81 (5), 1187–1195.
Ripley, E.M., Park, Y.R., Li, C., Naldrett, A.J., 2000. Oxygen Isotope Studies of the Voisey's Bay Ni-Cu-Co Deposit, Labrador, Canada. Econ. Geol. 95 (4), 831–844.
Rubatto, D., Gebauer, D., 2000. Use of Cathodoluminescence for U-Pb Zircon Dating by Ion Microprobe: Some Examples from the Western Alps. Springer, Berlin Heidelberg, pp. 373–400.
Sino Shaanxi Nuclear Industry Group Geological Survey Co, Ltd, 2014. The Survey Report of the Kaimuqi Mafic-Ultramafic Intrusion. pp. 1–156 (in Chinese with English abs.).
Sláma, J., Košler, J., Condon, D.J., Crowley, J.L., Gerdes, A., Hanchar, J.M., Horstwood, M.S.A., Morris, G.A., Nasdala, L., Norberg, N., 2008. Plešovice zircon — a new natural reference material for U–Pb and Hf isotopic microanalysis. Chem. Geol. 249, 1–35.
Song, X.Y., Keays, R.R., Zhou, M.F., Qi, L., Ihlenfeld, C., Xiao, J.F., 2009. Siderophile and chalcophile elemental constraints on the origin of the Jinchuan Ni-Cu-(PGE) sulfide deposit, NW China. Geochim. Cosmochim. Acta 73 (2), 404–424.
Song, X.Y., Yi, J.N., Chen, L.M., She, Y.W., Liu, C.Z., Dang, X.Y., Yang, Q.A., Wu, S.K., 2016. The giant Xiarihamu Ni-Co sulfide deposit in the East Kunlun Orogenic belt, Northern Tibet Plateau, China. Econ. Geol. 111, 29–55.
Sun, S.S., McDonough, W.F., 1989. Chemical and isotopic systematics of oceanic basalts: implications for mantle composition and processes. Geol. Soc. Lond., Spec. Publ. 42, 313–345.
Sun, Y., Zhang, G., Wang, J., Zhan, F., Zhang, Z., 2004. $^{40}Ar/^{39}Ar$ age of the basic sill swarms of two periods in the junctions area of Qinling and Kunlun and its tectonic significance. Acta Geol. Sin. 78, 65–71 (in Chinese with English abs.).
Tang, Z., Yan, H., Jiao, J., Li, X., 2005. New Classification of Magmatic Sulphide Deposits in China and Metallogenesis Related to Small Intrusions. Springer, Berlin Heidelberg, pp. 57–59.
Tang, Z., Yan, H., Jiao, J., Pan, Z., 2007. Regional metallogenic controls of small-intrusion-hosted Ni-Cu (PGE) ore deposits in China. Earth Sci. Front. 14 (5), 92–101.
Wall, C.J., Scoates, J.S., 2016. High-precision U-Pb zircon-baddeleyite dating of the JM reef platinum group element deposit in the Stillwater Complex, Montana (USA). Econ. Geol. 111 (3), 771–782.
Wang, G., 2014. Metallogenesis of nickel deposits in Eastern Kunlun Orogenic Belt, Qinghai Province. Jilin University Doctoral Dissertation. pp. 1–200 (in Chinese with English abs.).
Wang, G., Sun, F., Li, B., Li, S., Zhao, J., Yang, Q., Ao, C., 2013. Zircon U-Pb geochronology and geochemistry of the Early Devonian syenogranite in the Xiarihamu ore district from East Kunlun, with implications for the geodynamic setting. Geotecton. Metallog. 37, 685–697 (in Chinese with English abs.).
Wang, B.Z., Jing, C., Luo, Z.H., Chen, F.B., Tao, W., Guo, G.E., 2014. Spatial and temporal distribution of Late Permian-Early Jurassic intrusion assemblages in eastern Qimantag, East Kunlun, and their tectonic settings. Acta Petrol. Sin. 30, 3213–3228 (in Chinese with English abs.).
Wang, Y.L., Zhang, Z.W., Zhang, J.W., Qian, B., Liu, Y.G., You, M.X., 2017. Early mesozoic mantle-derived magmatic events and their geological significance in the East Kunlun Orogenic belt. Geol. Explor. 53, 855–866 (in Chinese with English abs.).
Wei, B., Wang, C.Y., Li, C., Sun, Y., 2013. Origin of PGE-depleted Ni-Cu sulfide mineralization in the Triassic Hongqiling no. 7 orthopyroxenite intrusion, Central Asian orogenic belt, northeastern China. Econ. Geol. 108 (8), 1813–1831.
Weis, D., Kieffer, B., Maerschalk, C., Barling, J., Jong, J.D., Williams, G.A., Hanano, D., Pretorius, W., Mattielli, N., Scoates, J.S., 2013. High-precision isotopic characterization of USGS reference materials by TIMS and MC-ICP-MS. Geochem. Geophys. Geosyst. 7, 139–149.
Wendlandt, R.F., 1982. Sulfide saturation of basalt and andesite melts at high pressures and temperatures. Am. Mineral. 67, 877–885.
Wiedenbeck, M., Alle, P., Corfu, F., Griffin, W., Meier, M., Oberli, F., Quadt, A.V., Roddick, J., Spiegel, W., 1995. Three natural zircon standards for U-Th-Pb, Lu-Hf, trace element and REE analyses. Geostand. Newslett. 19, 1–23.
Xiao, P., Gao, X., Hu, Y., Xie, C., Guo, L., Xi, R., Dong, Z., Kang, L., 2014. Study on the Geological Background of the Metallogenic Belt in the Western Section of the Altun - East Kunlun Mountains. Geological Publishing House, Beijing, pp. 1–261 (in Chinese).
Xiong, F.H., Ma, C.Q., Zhang, J.Y., Liu, B., Jiang, H.A., 2014a. Reworking of old continental lithosphere: an important crustal evolution mechanism in orogenic belts, as evidenced by Triassic I-type granitoids in the East Kunlun orogen, Northern Tibetan Plateau. J. Geol. Soc. 171, 847–863.
Xiong, F.H., Ma, C.Q., Jiang, H.A., Liu, B., Huang, J., 2014b. Geochronology and geochemistry of Middle Devonian mafic dykes in the East Kunlun orogenic belt, Northern Tibet Plateau: implications for the transition from Prototethys to Paleotethys orogeny. Chem. Erde 74, 225–235.
Yan, J.M., Sun, F.Y., Chen, G.J., Qian, Y., Li, L., Wang, C., He, S.Y., 2016. Geochemical characteristics of gabbro from Binggounan Cu–Ni deposit in the north of eastern Kunlun metallogenic belt. Global Geol. 35, 729–737 (in Chinese with English abs.).
Yang, J.S., Wang, X.B., Shi, R.D., Xu, Z.Q., Wu, C.L., 2004. The Dur'ngoi ophiolite in east Kunlun, northern Qinghai-Tibet Plateau: a fragment of paleo-Tethyan oceanic crust. Geol. China 31, 225–239.
Yang, L., Zhou, H.W., Zhu, Y.H., Dai, X., Lin, Q.X., Ma, Z.Q., Jian, K.K., Zhang, M.Y., 2014. Geochemical characteristics and LA-ICP-MS zircon U-Pb ages of intermediate to mafic dyke swarms in Haxiya area, Golmud, Qinghai Province. Geol. Bull. China 33, 804–819 (in Chinese with English abs.).
Yang, S., Yang, G., Qu, W., Du, A., Hanski, E., Lahaye, Y., Chen, J., 2018. Pt-Os isotopic constraints on the age of hydrothermal overprinting on the Jinchuan Ni-Cu-PGE deposit, China. Mineral. Deposita 53, 757–774.
Ye, H.M., Li, X.H., Lan, Z.W., 2013. Geochemical and Sr–Nd–Hf–O–C isotopic constraints on the origin of the Neoproterozoic Qieganbulake ultramafic–carbonatite complex from the Tarim Block, Northwest China. Lithos 182-183, 150–164.
Zhang, M.J., Kamo, S.L., Li, C.S., Hu, P.E., Ripley, E.M., 2010. Precise U–Pb zircon–baddeleyite age of the Jinchuan sulfide ore-bearing ultramafic intrusion, western China. Mineral. Deposita 45, 3–9.
Zhang, J.Y., Ma, C.Q., Xiong, F.H., Liu, B., Li, J.W., Pan, Y.M., 2014. Early Paleozoic high-Mg diorite-granodiorite in the eastern Kunlun Orogen, western China: Response to continental collision and slab break-off. Lithos 210-211, 129–146.
Zhang, Z.W., Tang, Q.Y., Li, C.S., Wang, Y.L., Ripley, E.M., 2017. Sr-Nd-Os-S isotope and PGE geochemistry of the Xiarihamu magmatic sulfide deposit in the Qinghai–Tibet

plateau, China. Mineral. Deposita 52, 51–68.
Zhang, Z.W., Wang, Y.L., Qian, B., Liu, Y.G., Zhang, D.Y., Lü, P.R., Dong, J., 2018. Metallogeny and tectonomagmatic setting of Ni-Cu magmatic sulfide mineralization, number I Shitoukengde mafic-ultramafic complex, East Kunlun Orogenic Belt, NW China. Ore Geol. Rev. 96, 236–246.
Zhou, W., 2016. Petrogenesis of Shitoukengde mafic-ultramafic intrusion and analysis of its metallogenic potential, East Kunlun. Chang'an University Master's Degree Thesis. pp. 1–99 (in Chinese with English abs.).
Zhu, Y., Lin, Q., Jia, C., Wang, G., 2006. SHRIMP zircon U-Pb age and significance of early Paleozoic volcanic rocks in East Kunlun orogenic belt, Qinghai Province, China. Sci. China Earth Sci. 49, 88–96.
Zientek, M., Cooper, R., Corson, S., Geraghty, E., 2002. In: Cabri, L.J. (Ed.), Platinum-group Element Mineralization in the Stillwater Complex, Montana. The Geology, Geochemistry, Mineralogy and Mineral Beneficiation of Platinum-Group Elements. Canadian Institute of Mining, Metallurgy and Petroleum, pp. 459–481 (this volume).